

Student thesis series INES nr 404

Monitoring of Santorini (Greece) volcano during post-unrest period (2014-2016) with Interferometric Time series of Sentinel-1A

Christos Bountzouklis

2016
Department of
Physical Geography and Ecosystem Science
Lund University
Sölvegatan 12
S-223 62 Lund
Sweden



Christos Bountzouklis (2016).

Monitoring of Santorini (Greece) volcano during post-unrest period (2014-2016) with Interferometric Time series of Sentinel-1A

Master degree thesis, 30 credits in *Geomatics*

Department of Physical Geography and Ecosystem Science, Lund University

Level: Master of Science (MSc)

Course duration: *January* 2016 until *September* 2016

Disclaimer

This document describes work undertaken as part of a program of study at the University of Lund. All views and opinions expressed herein remain the sole responsibility of the author, and do not necessarily represent those of the institute.

Monitoring of Santorini (Greece) volcano during post-unrest period (2014-2016) with Interferometric Time series of Sentinel-1A

Christos Bountzouklis

Master thesis, 30 credits, in *Geomatics*

Supervisor 1 Issaak Parcharidis
Department of Geography, Harokopio University, Greece

Supervisor 2 Karlis Zalite
Department of Physical Geography and Ecosystem Science,
Lund University, Sweden

Exam committee:

Per-Ola Olsson, Department of Physical Geography and Ecosystem
Science, Lund University, Sweden

Ulrik Mårtensson, Department of Physical Geography and Ecosystem
Science, Lund University, Sweden

Table of Contents

| | |
|---|-----------|
| Table of Contents..... | IV |
| List of Figures..... | V |
| List of Tables..... | V |
| Abbreviations..... | VI |
| Acknowledgments..... | VII |
| Abstract..... | VIII |
| 1. Introduction..... | 1 |
| 1.1 Background..... | 1 |
| 1.2 Study Area..... | 2 |
| 1.3 Aim & Scientific Objectives..... | 4 |
| 1.4 Thesis Outline..... | 5 |
| 2. Literature Review..... | 7 |
| 2.1 InSAR Applications..... | 7 |
| 2.2 Santorini Volcano InSAR Monitoring..... | 10 |
| 3. Data & Methodology..... | 13 |
| 3.1 SAR Principles..... | 13 |
| 3.1.1 InSAR Principles..... | 16 |
| 3.2 Data..... | 19 |
| 3.2.1 Sentinel 1 - Copernicus Program..... | 19 |
| 3.2.2 Global Positioning System (GPS) Data..... | 21 |
| 3.3 Methodology..... | 23 |
| 3.3.1 Processing & Stack Formation..... | 24 |
| 3.3.2 Inteferometric Stacking (IS)..... | 28 |
| 3.3.3 Singular Value Decomposition (SVD)..... | 29 |
| 4. Results..... | 31 |
| 4.1 Deformation maps based on the IS method..... | 31 |
| 4.2 Deformation maps based on the SVD method..... | 34 |
| 4.3 GPS velocity maps..... | 36 |
| 4.4 InSAR Time Series..... | 38 |
| 4.5 InSAR & GPS Time Series comparison..... | 40 |
| 5. Discussion-Interpretation..... | 43 |
| 6. Conclusions..... | 49 |
| 7. References..... | 51 |

List of Figures

| | |
|---|----|
| Figure 1 Santorini and its local seismic activity. | 3 |
| Figure 2 SAR Imaging geometry. | 13 |
| Figure 3 The foreshortening effect | 14 |
| Figure 4 The layover effect..... | 15 |
| Figure 5 The radar shadow effect | 15 |
| Figure 6 Geometry of a satellite interferometric SAR system..... | 16 |
| Figure 7 Principle of DInSAR for deformation measurement..... | 18 |
| Figure 8 - Sentinel-1A SLC bursts and SLC mosaic | 21 |
| Figure 9 GPS stations location of the | 22 |
| Figure 10 Interferometric processing flow chart. | 23 |
| Figure 11 Miss-registration offsets ascending dataset. | 25 |
| Figure 12 Miss-registration offsets descending dataset. | 25 |
| Figure 13 Interferogram network plots. | 26 |
| Figure 14 Average coherence images in SAR Geometry. | 27 |
| Figure 15 Displacement visible to the LOS of the ascending and descending views.. | 31 |
| Figure 16 Average LOS (descending) deformation using the IS method..... | 32 |
| Figure 17 Average LOS (ascending) deformation using the IS method..... | 33 |
| Figure 18 Average LOS (descending) deformation using the SVD method | 34 |
| Figure 19 Average LOS (ascending) deformation using the SVD method | 35 |
| Figure 20 Horizontal GPS ground velocity map..... | 36 |
| Figure 21 Vertical GPS ground velocity map..... | 37 |
| Figure 22 InSAR Time Series LOS (descending) displacement. | 38 |
| Figure 23 InSAR Time Series LOS (ascending) displacement | 39 |
| Figure 24 InSAR Time Series LOS displacement on station “SANT”. | 40 |
| Figure 25 GPS time series depicting the ground velocities on station “SANT” | 41 |
| Figure 26 Local seismic events during the study period..... | 44 |
| Figure 27 2-Dimensional deformation profile (A-B) over Nea Kameni | 45 |
| Figure 28 2-Dimensional deformation profile (C-D) over Nea Kameni | 46 |

List of Tables

| | |
|---|----|
| Table 1: Modelled position of point source ground for the unrest period | 11 |
| Table 2: Sentinel 1A data description. | 21 |
| Table 3: GPS stations information | 22 |
| Table 4: GPS stations measured velocities | 37 |

Abbreviations

DEM- Digital Elevation Model

DInSAR- Differential Interferometry Synthetic Aperture Radar

EO- Earth Observation

ESA- European Space Agency

GNSS - Global Navigation Satellite System

GPS- Global Positioning System

InSAR- Interferometry Synthetic Aperture Radar

ISMOSAV- Institute for the Study and the Monitoring of the Santorini Volcano

MCF- Minimum Cost Flow

LOS- Line of Sight

SAR- Synthetic Aperture Radar

SLC- Single Look Complex

SVC- Santorini Volcanic Complex

TOPSAR-Terrain Observation with Progressive Scans SAR

Acknowledgments

Some people contributed decisively to complete my thesis and so i must thank them individually. Firstly, I would like to thank my supervisors. Prof. Issaak Parcharidis from the Department of Geography at Harokopio University of Athens, for suggesting the topic, cooperating, guiding and advising me as an external supervisor. Also, Researcher Dr. Karlis Zalite from the Department of Physical Geography and Ecosystems Science at Lund University, for assisting me as a second supervisor. His comments, ideas and corrections greatly improved my thesis and helped me understand even further the aspects of radar remote sensing.

Additionally, I would like to express my gratitude to my colleague and friend Stefanos Georganos for his valuable assistance and support throughout the whole duration of the preparation of this thesis. Undoubtedly, I must thank my friends and classmates Jayan Wijesingha and Abdalla Eltayeb for their company and mutual understanding during our studies. Most of all, I would like to thank my partner Marie for encouraging, understanding and assisting me the relentlessly. Lastly, I'm deeply grateful to my family for their help and support they provided during my studies

Abstract

Ground deformation monitoring is one of the main geoindicators that should be considered to assess volcanic hazard. Satellite earth observation data and Synthetic Aperture Radar (SAR) interferometry have been used continuously since 1992 to measure or study the temporal evolution of surface deformation in volcanic areas in conjunction with ground-based geodetic measurements. Such monitoring methods were applied to study the current state of Santorini Volcanic Complex (Greece). During the period 1992-2010 the volcano was characterized by the gradual deflation of the volcanic island Nea Kameni. However, at the beginning of 2011 the volcano displayed signs of unrest with increased microseismic activity and significant ground uplift. A gradual decrease of inflation rates within the first quarter of 2012 was confirmed from subsequent observations and thus indicating that the volcano entered a post-unrest period. The ongoing post-unrest period, was examined using 89 Sentinel-1A satellite scenes covering the period October 2014 to June 2016. Exploiting the capabilities of DInSAR techniques like the Interferometric Stacking (IS) and the Singular Value Decomposition(SVD) algorithm, several deformation maps and time series graphs were produced to illustrate the status of the volcano. Interferometric results show that the volcano displays a relative uniform surface deformation with low uplifting rates, horizontal velocities and interesting alterations in the deformation pattern through time, with the decrease of microseismicity in the area.

Keywords: Volcanic Hazard, SAR Interferometry, Earth Observation, Santorini Volcanic Complex, Sentinel-1A

1. Introduction

1.1 Background

The number of earth observation (EO) satellites in the last years has multiplied and the availability of the data to the public has become much easier, providing scientists with the ability to integrate ground surveillance data with satellite derived information to characterise phenomena during natural disasters. Many countries worldwide are affected by at least one major natural hazard such as floods, fires, sandstorms, earthquakes, volcanic eruptions, landslides, rapid vertical ground displacements, and by risks related to man-made activities such as chemical and nuclear accidents. These risks can be mitigated through better prevention and preparedness that includes provision and better use of space-based assets (Bignami 2012). In particular, satellite remote sensing has proved its potential as a powerful and reliable tool to monitor volcanic activity and more specifically the use of satellite radar data and the application of SAR Interferometry. Over the years, a large number of applications for monitoring volcanoes have been demonstrated, with excellent results (Massonnet et al. 1995; Briole et al. 1997; Lanari 1998; Amelung et al. 2000; Hooper et al. 2004; Fournier et al. 2010 Antonielli et al. 2014).

Synthetic Aperture Radar (SAR) is a powerful remote sensing radar system used for earth observation applications (Curlander and McDonough, 1991). The sensor emits electromagnetic radiation and then coherently records the amplitude and phase of the returned signal to produce images of the ground. Interferometric Synthetic Aperture Radar (InSAR) is a recognized and established remote sensing technique that directly measures the phase change between two or more SAR phase images acquired at different times of the same ground pixels of the Earth's surface. Consequently, the detection and mapping of changes of spatial and/or dielectric properties of the ground surface by using differences in the phase of the waves returning to the satellite or aircraft is made possible.

When a series of SAR phase images are available over the same area, combining them into a series of differential interferograms allows us to monitor displacement trends through time, resulting in multitemporal InSAR (Zhou et al. 2009). The produced interferogram is an image formed by the phase difference of two properly coregistered SAR images of the same area. The result is measured in radians (phase) and

visualized as lines of equal phase which are called “fringes”. The number of fringes in an interferogram is counted from a reference point where the surface deformation is supposedly zero. The time interval between the two SAR image acquisitions can vary from a few seconds to years, depending on how fast the target area undertakes changes.

During the past decades, the use of SAR Interferometry to monitor ground deformation has become widely recognized and has been improved extensively (from centimetre to millimetre resolution), proving to be a technique that can be extremely useful as a remote sensing tool (Rosen et al. 2000; Ferretti et al. 2001; Hanssen 2004).

1.2 Study Area

Santorini is located in the Aegean Sea, Greece and it is the most southern part of the group of islands called Cyclades. Santorini consists of a smaller group of five islands which are Fira, Thirasia, Aspronisi, Palea and Nea Kameni (volcanic islands) (Figure 1). The main island is Fira (Thera), which covers an area of 73 sq. km. and its population is approximately 15,000 people which are distributed among thirteen villages, with many of them situated on near-vertical encompassing cliffs.

Currently, Santorini is one of the most popular touristic destinations and widely known around the world for its spectacular view, architecture, gastronomy, sunset and its uniquely formed beaches. In the scientific community, Santorini is one of the most well-researched volcanoes in the world and of course is widely known for playing a critical role in shaping the human history in the area around it. Due to the existence of the active volcano, the island is constantly monitored by a thermal, seismic, chemical and topographic network, with stations scattered around the island which are operated by the Institute for the Study and Monitoring of the Santorini Volcano (I.S.M.O.S.A.V.), which is a non-profit organization, founded in 1995.

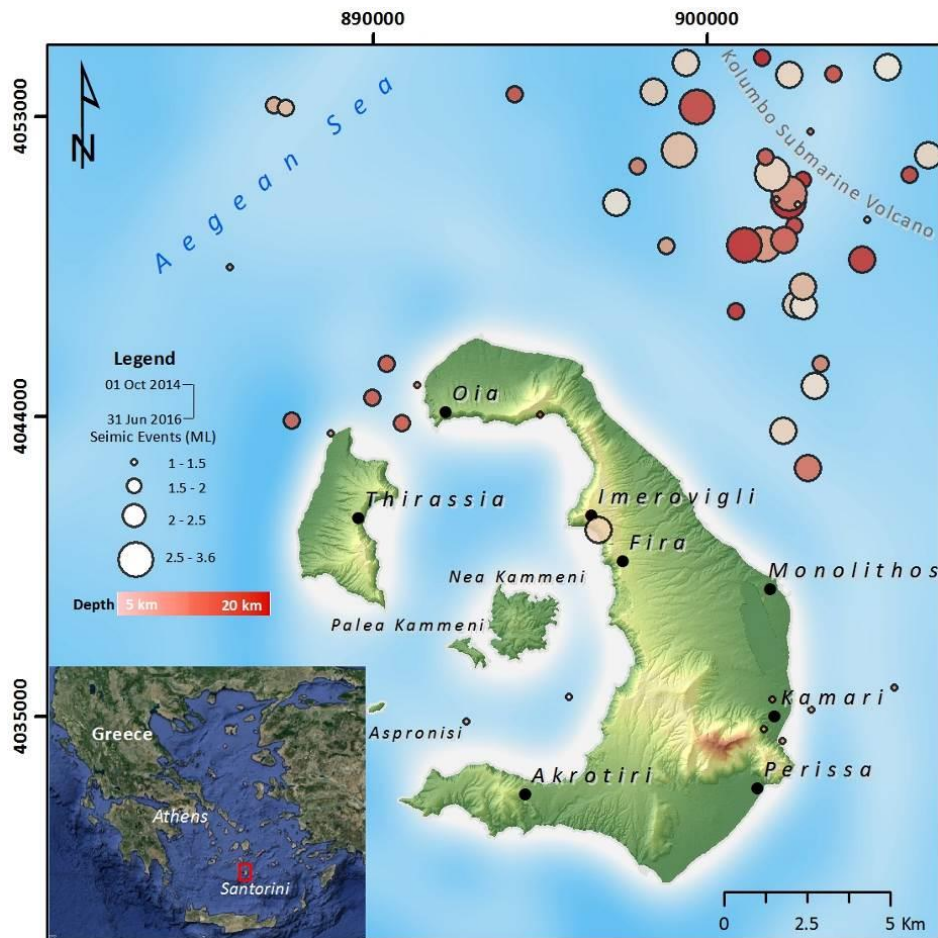


Figure 1 Santorini and its local seismic activity.

The island is part of the South Aegean Volcanic Arc (or Hellenic arc) which extends almost 500 km from mainland Greece to Turkey. The trench is formed by subduction of the African plate, which lies about 250 km south of the arc, under the Eurasian tectonic plate. Also, the same subduction process is responsible for the magmagenesis which has resulted in the formation of the volcanic arc. Even though Santorini is the most active and well-known volcano of the arc, there are other volcanic centers like Aegina, Methana, Poros, Milos, Kos, Yali and Nisyros.

The caldera (volcanic crater) in Santorini is 11 kilometres long and is a mostly submerged volcanic complex that is part of a well-developed and very active system that began its volcanic history about 600 thousand years ago, due to subduction along the Hellenic arc (Druitt et al. 1999). Moreover, the volcano is considered as one of the potentially most dangerous volcanoes in Europe (Druitt et al. 1999), and has produced many volcanic events until now, with the most recent one in January 1950 which was insignificant in comparisons to older ones. The most powerful eruption of the volcano 3600 years ago, and one of the most powerful volcanic events in recorded history, was

the so called Minoan eruption which not only destroyed part of the island but also resulted to the collapse of the Minoan civilization (McCoy and Heiken, 2000; Manning et al. 2006) by the tsunamis that were created by the eruption. In addition, according to the results of a recent marine survey (Sigurdson et al. 2006) the Minoan eruption was much bigger than the scientists initially believed and is now considered as equal in volume to the largest known historical eruption, that of Tambora in Indonesia in 1815 (Sigurdsson and Carey, 1989).

Finally, the composition of the volcanic islands has changed many times the last 2200 years. Each time a minor eruption was taking place it had as a result the emerging of lava from the sea and the forming of new land. This process was studied by many scientists the past years regarding the time and the place of the emergence of lava to form the current shape (Georgalas 1962; Huijismans 1985; Druitt et al. 1999; Pyle & Elliott 2006; Nomikou et al. 2014)

1.3 Aim & Scientific Objectives

The aim of this study is to determine the characteristics of the ground deformation at Santorini Volcanic Complex, during the post-unrest period (2014-2016) by exploiting Sentinel-1A data. The post-unrest period is anticipated to have considerable lower rates of deformation and decrease of the microseismic activity comparing to the unrest period that occurred between February 2011 to May 2012 and presented a significant amount of uplift in the volcanic island Nea Kameni as well as in Imerovigli and Fira (Thera island). In total, 89 Sentinel-1A acquisitions were processed and 476 interferograms were formed spanning the period between October 2014 and June 2016. Moreover, ground based geodetic observations were used to compare interferometric results which were produced based on Sentinel-1A data.

Scientific Objectives:

- i. Create deformation maps for the post unrest period (2014-2016)
- ii. Create deformation time series diagrams for the post unrest period (2014-2016)
- iii. Compare interferometric results with ground geodetic measurements.

- iv. Assess the efficiency and the functionality of Sentinel-1A data for volcano monitoring.

The outcomes of the study would be of great interest to scientists who study and monitor volcanic activity, research groups which deal with InSAR applications and local policy makers. Also, scientists who are interested in using Sentinel-1 data for InSAR applications can have an example basis from this project.

1.4 Thesis Outline

Chapter 1-Introduction: Gives an overall overview of the thesis and presents the motivation and the research questions. Also, it presents some information about the history, the geology and the geography of the study area.

Chapter 2-Literature Review: Includes a few major applications of SAR Interferometry to monitor different natural disasters and measure displacement, as well as past results using the similar techniques and methods for different periods in the same area to monitor the volcano's movements.

Chapter 3-Data&Methodology: Describes the details about the amount, type and basic information about the satellite data that were used. Additionally, it describes the general idea of SAR Interferometry and how it is applied as well as the methodology on which the processing was based on.

Chapter 4-Results: Presents the results produced by the processing of the data in the form of maps and time series graphs. Also, it includes the comparison of InSAR results with GPS measurements.

Chapter 5-Discussion: Clarifies the interpretation of the demonstrated results and relates the outcomes of the thesis with the scientific objectives that were set in the start. Furthermore, proposals for further investigation and improvements for more accurate and robust results are also discussed.

Chapter 6-Conclusions: Presents the extracted conclusions and summarizes the key points and the outcomes of the project.

2. Literature Review

2.1 InSAR Applications

The fields in which InSAR can be applied are very broad and rapidly expanding throughout the years:

-In *seismology*: land surface deformation caused by earthquake events; Funning et al. (2005) analyzed SAR Interferograms formed by Envisat ASAR data in order to construct a three-dimensional displacement field of the deformation due to the 2003 earthquake in Bam (Iran). The results of their modeling displayed that the majority of the fault motion observed by InSAR occurred on two faults, a hidden strike-slip fault extending under the center of Bam, and a second, obliquely slipping fault whose surface trace is close to the previously mapped Bam Fault. Furthermore, the geometry of these two faults, which according to the authors, are likely to intersect and interact at depth, is similar to that proposed for other earthquakes in eastern Iran.

Calais et al. (2010) studied the 7.0 Mw earthquake in Port-au-Prince region of Haiti in 2010 using a combination of geodetic (GPS), and remote-sensing (InSAR) techniques. The measurements of ground motion showed that the earthquake involved a combination of horizontal and contractional slip, causing transpressional motion. Moreover, there was an unexpected contractional deformation caused by the earthquake while the pattern of strain accumulation indicated present activity on faults other than the known ones in the area. Instead, the authors discovered that the earthquake ruptured from an unmapped north-dipping fault, called the Léogâne fault. Interferometry measurements of ground motion showed that the earthquake involved a combination of horizontal and contractional slip, causing transpressional motion. This result is consistent with the long-term pattern of strain accumulation in Hispaniola. The unexpected contractional deformation caused by the earthquake and by the pattern of strain accumulation indicates present activity on faults other than the Enriquillo–Plantain Garden fault.

-In *natural disaster monitoring and assessment*: volcanoes and landslide movement; Monitoring volcanic activity through interferometric techniques was one of the first fields of appliance with trustworthy results (Massonnet et. al 1995). An example of the method used in volcanology is a study of Mt. Etna in Italy, which was carried out from Solaro et al. (2010). The study period ranged from 1994 to 2008 and included

the usage of data acquired from multiple sensors such as ERS-1/2 and Envisat. The results acquired by processing the SAR data, were separated in different periods of activity and fault mechanisms. Additionally, they showed widespread instability of the flanks, which was by far the predominant type of deformation at Mt. Etna regardless of the state of the volcano (magma storage, dike emplacement, inactivity).

Concerning other natural disasters monitoring, Liu et al. (2012) investigated major landslide hazards in the Three Gorges region of China by employing InSAR time series. The data used in the study include three different groups of Envisat ASAR images (85 in total), which were processed separately. The resulted maps demonstrated that the InSAR time-series technique successfully identified the surface deformation in the study area by showing consistent linear movement trends which enabled the identification of two distinct landslides with different moving patterns and magnitudes.

-In *glaciology*: ice sheet motion and rheology, glacier flow, postglacial rebound of the lithosphere; Quincey et al. (2009) published a study which involved the quantification of the glacier velocities in Everest using ERS-1 and ERS-2 data between 1992 and 2002. The results demonstrated that nineteen out of twenty glaciers under examination were stable or very close to be stable. The authors concluded that InSAR was successfully employed to measure glacier velocities across the study area and suggested the constant monitoring of such areas using the same methods.

Strozzi et al. (2008) used L-band SAR data acquired by the JERS-1 satellite between 1994 and 1998 to estimate glacier motions in the Arctic. The ice-surface displacement maps showed that the ice caps of Svalbard, Novaya Zemlya and Franz-Josef Land are divided into a number of clearly defined fast-flowing units. In addition, the produced results are in general agreement with previous studies performed using different satellite data and geodetic techniques.

-In *mining*: land subsidence due to mining; Paradella et al. (2014) analyzed a stack of 33 TerraSAR-X images which provided a synoptic and informative view of the deformation processes affecting the Carajás complex (Brazil) due to mining activities. Deformation maps illustrated that most of the mining complex was stable during the time span of the TerraSAR-X coverage, but high deformation rates were detected over waste dumps and some pit slopes. Moreover, the authors concluded that the

complementary use of space-based SAR along with field monitoring systems proved to be strategic for operational mining planning and risk assessment. Linlin et al. (2007) using a series of ERS-1, ERS-2, and JERS-1 radar images for the interferometric processing, demonstrated the ability of Differential Synthetic Aperture interferometry (DInSAR) to locate the affected areas caused by mine subsidence in a vegetated region in New South Wales (Australia). The results showed that for mine subsidence monitoring, the JERS-1 (longer wavelength) data are more robust in the presence of vegetated or agricultural ground cover, and also more suitable for areas experiencing high rate ground deformation, compared to ERS-1/ERS-2 (shorter wavelength) data. However, data of shorter wavelength are much more sensitive to mine subsidence. Lastly, the authors emphasized that with the proper atmospheric corrections, the technique is a cost-effective, reliable, and an operational complement to traditional ground survey methods.

-In *environmental and structural engineering*: ground subsidence and structural stability; Parcharidis et al. in 2015 assessed the stability over Rio-Antirio(Greece) multispan-cable-stayed bridge as well as the surrounding area. Using Envisat ASAR and TerraSAR-X StripMap satellite data, they managed to extract qualitative information on the temporal displacement pattern of the Rio-Antirio Bridge as well as quantitative measurements regarding the rates of deformation accumulation. The consequences of the results are fruitful because, as it was shown, the methodology used can also be applied to other cases, such as dams, which are exposed to risks.

Di Martire et al. in 2014 presented an application of DInSAR algorithms to monitor the ground deformation of Conza Dam, located in the southern Apennines (Italy). The analysis was carried out using 51 Envisat ASAR images and they concluded that there is a high agreement between the final DInSAR displacements and in-situ instrumental data, which clearly demonstrates the reliability of the technique for the precise monitoring of civil infrastructures, and concretely, in dams with a high exposure factor and its consequent risk.

-In *forestry*: forest canopy height, forest mapping and monitoring; Askne et al. in 2013 using eighteen interferometric Synthetic Aperture Radar (SAR) image pairs, between June 2011 and August 2012, acquired from the TanDEM-X mission, investigated the spatial distribution and estimation accuracy of biomass over the hemi-boreal test site of Remningstorp in Sweden. The presented analysis

demonstrated that TanDEM-X InSAR data together with an accurate high-resolution Digital Terrain Model (DTM) have a potential to estimate above-ground dry biomass with high accuracy in the case of forest conditions like those in Remningstorp.

-In *ground water hydrology*: land subsidence due to excess water pumping or uplift due to ground water recharge; In 2003, a study by Raucules et al. was conducted in order to monitor the urban subsidence in the city of Prato (Italy) caused by excessive water pumping for industrial reasons. To achieve that, the research team used six ERS-1 and ERS-2 images to form four interferograms during the period of 1993-2000. Based on those interferometric combinations, the subsidence phenomenon in the area appeared to be constant with a maximum value of about 8.3 cm throughout the seven-year period. The authors conclude that InSAR could play a significant role in land use planning and natural risk assessment.

2.2 Santorini Volcano InSAR Monitoring

A plethora of studies have been carried out to monitor the movement of the volcano in Santorini using different geodetic techniques over the past years. With the development of satellite interferometry, scientists obtained another reliable tool to measure the displacement, observe the deformation pattern and validate or merge any other results acquired with different methods. Most of the studies which included interferometric results for the study area were published in the last five years, which is to be expected since the unrest period of the volcano started in late December 2010 to January 2011. During the rest period (1950-2010) the volcano remained quiet, with no documented reports of seismic activity. Since the availability of SAR data for the area started in 1992, both the rest (1992-2010) and unrest period (2011-2012) was studied by many research teams, using image acquisitions from multiple sensors such as ERS-1/2, Envisat, TerraSAR-X, ALOS and RADARSAT-2. In addition, most of the studies included comparisons and integration of InSAR and GPS results (Foumelis et al., 2013; Lagios et al., 2013; Parks et al., 2015) in order to get a better overview and robust conclusions in regards to the volcano's movement.

Regarding the rest period, the ground deformation at the centre of the caldera (N. Kameni) was measured ranging from around 5 to 6 mm per year of subsidence (Papageorgiou et al. 2012; Foumelis et al. 2013; Lagios et al. 2013; Parks et al. 2015). over the 18-year period. According to the results, no other part of the SVC was

showing any significant displacement. However, the first significant activity of the volcano since 1950 was reported in the beginning of January 2011 when the volcano entered the unrest period which was mainly characterized by the increase of micro-seismicity inside the caldera and extended ground uplift (Newman et al. 2012).

An important observation was made from Foumelis et al. (2013), by processing ALOS PALSAR data which indicated the onset of the phenomenon in mid-2010, where an aseismic pre-unrest phase of increased subsidence (1–3 cm) preceded the uplift. In addition, a gradual decrease of inflation rates within the first quarter of 2012 was confirmed from subsequent RADARSAT-2 observations. The unrest period lasted until the end of April of 2012 and during that time the observed mean SAR velocities showed a radial uplift of the entire volcanic complex, reaching a maximum local value of 14 cm (Newman et al. 2012, Parks et al. 2012, Foumelis et al. 2013, Lagios et al. 2013, Papoutsis et al. 2013, Parks et al 2015). However, because the magmatic source was modelled offshore in the northern part of the caldera and due to the submerged parts of the area, the maximum deformation is very likely to have been underestimated (Foumelis et al. 2013).

Previous research has used both GPS and InSAR measurements to model the location and depth of the deformation source of the observed inflation (Table 1). Using numerous techniques and algorithms like Interferometric Stacking, Singular Decomposition Value, SqueeSAR, Persistent Scatterer Interferometry (PSI) and Small Baseline Subset (SBAS) the scientists in the mentioned publications were able to track and measure the displacement over SVC using this relatively new and advanced remote sensing method with absolute success.

Table 1 *Modelled position of point source ground deformation based on InSAR and GPS measurements during the unrest period (2011-2012).*

| Publication | Method | Longitude (°E) | Latitude (°N) | Depth (km) |
|-----------------------|-----------------|-----------------------|----------------------|-------------------|
| Newman et al. 2012 | GPS | 25.389–25.390 | 36.423–36.430 | 3.9-4.0 |
| Parks et al. 2012 | InSAR | 25.389 | 36.430 | 4.4 |
| Papoutsis et al. 2013 | GPS | 25.384 | 36.429 | 3.5 |
| Papoutsis et al. 2013 | InSAR | 25.403 | 36.426 | 6.3 |
| Foumelis et al. 2013 | GPS | 25.389 | 36.424 | 4.0 |
| Foumelis et al. 2013 | InSAR | 25.389 | 36.429 | 4.3 |
| Foumelis et al. 2013 | Joint InSAR/GPS | 25.389 | 36.425 | 3.8 |
| Lagios et al. 2013 | InSAR | 25.395 | 36.426 | 4.5 |
| Lagios et al. 2013 | GPS | 25.389 | 36.426 | 4.9 |

| | | | | |
|-------------------|-----------------|--------|--------|-----------------------|
| Parks et al. 2015 | GPS | 25.390 | 36.428 | 4.4 ($\pm 0.5-0.6$) |
| Parks et al. 2015 | InSAR | 25.388 | 36.428 | 4.2 ($\pm 1.3/1.4$) |
| Parks et al. 2015 | Joint InSAR/GPS | 25.388 | 36.428 | 4.4 ($\pm 0.5/0.6$) |
| Median | - | 25.389 | 36.427 | 4.2 |

3. Data & Methodology

3.1 SAR Principles

Radar remote sensing offers some unique characteristics and benefits such as being weather or sunlight independent, but also presents some issues and particularities that need to be described to avoid confusion.

Unlike optical sensors, SAR imaging systems transmit and receive radiation right side-looking and along the track direction (Figure 2). This way of obtaining imageries enables two different viewing geometries (line of sight (LOS)), (a) the ascending, when the satellite moves from south to north and (b) the descending, when the satellite moves from north to south. The inclination of the antenna with respect to the nadir is called incidence angle and in most SAR systems it varies from 20° to 50° .

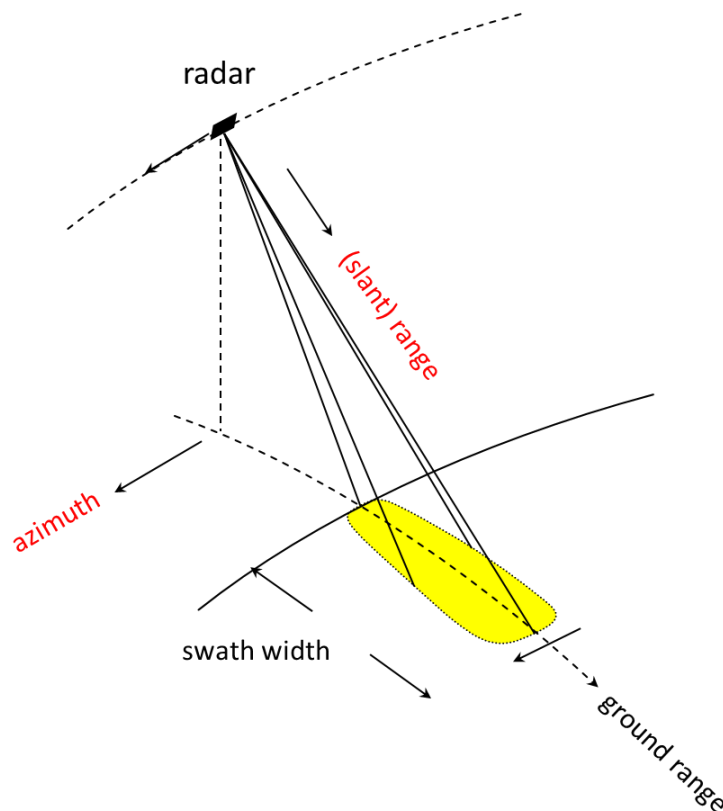


Figure 2 Imaging geometry of a typical side looking Synthetic Aperture Radar system (SAR-EDU - <https://saredu.dlr.de/>)

SAR images contain a measurement of the amplitude of the radiation backscattered toward the antenna by the objects (scatterers) contained in each SAR resolution cell.

The amplitude values depend on the orientation, roughness, size and the dielectric properties (e.g. water vs dry vegetation) of the scatterers on the earth's surface. Naturally, urban areas and rocky environments display strong amplitudes, while smooth flat surfaces like calm water, signify low amplitude values, since the radiation is mainly mirrored away from the radar. SAR instruments are coherent systems which can record not only the amplitude but also the phase of a recorded signal. The phase value is a measurement of the time that an echo transmitted from a radar antenna needs to reach the ground objects and then return to the radar. The phase is the key observable of all interferometric SAR techniques (Ferretti 2007). Additionally, radar instruments can be designed to transmit and receive waves in different orientations of the electric field. By altering the polarization of a transmitted signal, it is possible to obtain information on the polarimetric properties of the observed surfaces. Commonly, SAR systems are single-polarized, which means that they transmit either horizontally or vertical polarized waves and receive the same (HH or VV). However, there are SAR systems which can be fully polarimetric and operate in all polarization modes: HH, VV, HV, VH. Inevitably, due the configuration of the viewing angle of the earth's surface, many geometrical distortions are contained in SAR images which can lead to misinterpretations of the terrain and thus, it is essential to explain how these errors occur and how they affect the objects depicted in the images. These distortions are:

- i) *Foreshortening*: This effect causes the compression of the image which results to incorrect surface length representation. As can be seen in Figure 3, equal in length surfaces A-B, C-D will appear reduced (A' to B') or even zero (C' to D') in a radar image.

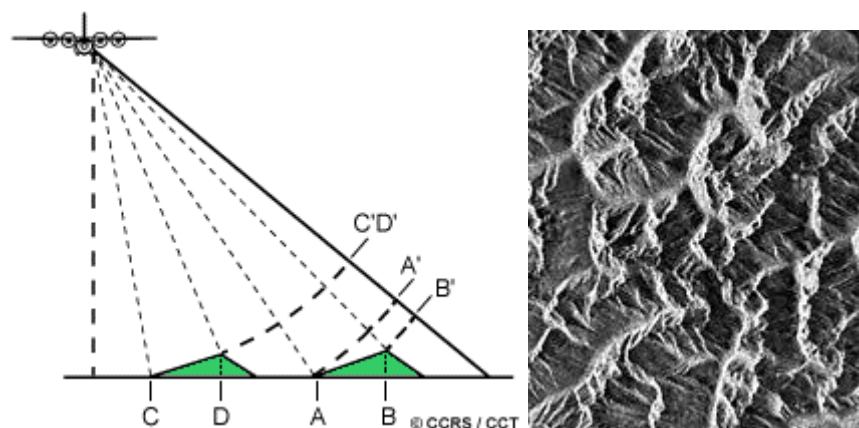


Figure 3 The foreshortening effect on mountainous terrain (Canada Centre for Mapping and Earth Observation - www.nrcan.gc.ca)

ii) *Layover*: this distortion occurs when the radar signal reaches the top of a mountain (B) before it reaches the base (A) which means that the signal from the top will return to the radar antenna earlier than the one from the base. This results to an inversion of the surface of mountainous areas when depicted in a radar image figure 4.

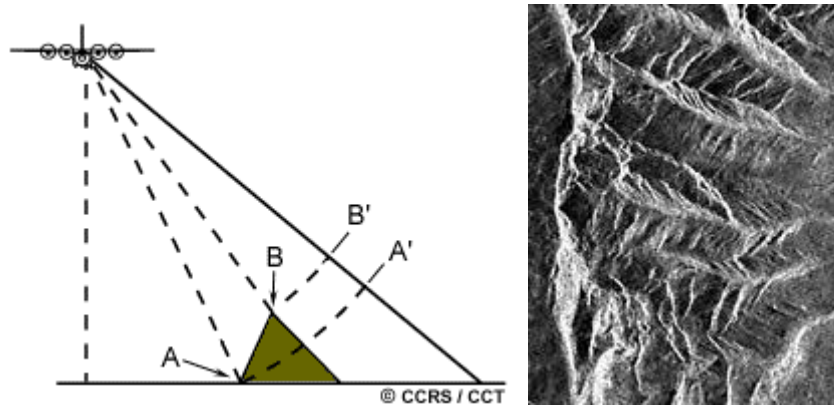


Figure 4 The layover effect on mountainous terrain (Canada Centre for Mapping and Earth Observation - www.nrcan.gc.ca)

iii) *Shadow*: Radar shadow appears when the radar beam is unable to illuminate parts of the ground surface due to their high angles. This effect causes vertical features or hilly terrain to appear dark in radar images since there is no energy available to backscatter. Red surfaces in figure 5 are shadowed and would contain no information in a radar image.

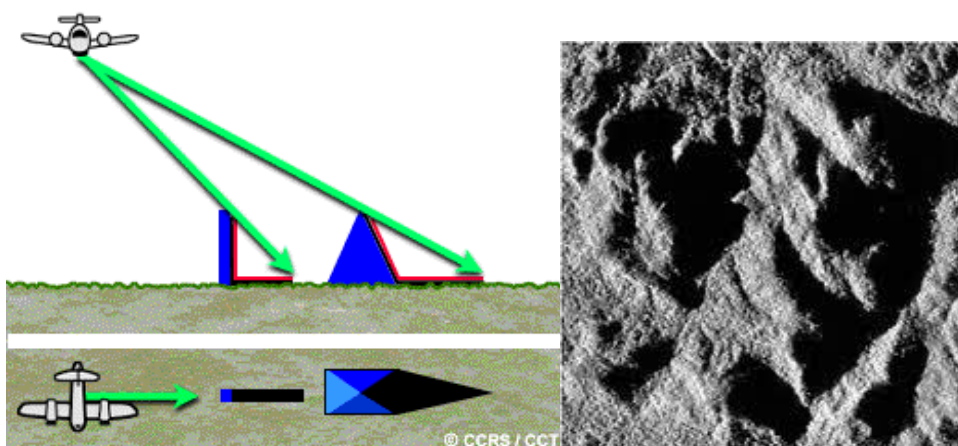


Figure 5 The radar shadow effect on hilly terrain (Canada Centre for Mapping and Earth Observation - www.nrcan.gc.ca)

3.1.1 InSAR Principles

➤ SAR Interferometry (InSAR)

As it was mentioned in the background, InSAR is a technique that measures the phase difference between two SAR phase images acquired at different times of the same ground pixels of the Earth's surface (Figure 6). Generally, there are two methods order to acquire an interferometric pair: a) single-pass interferometry and b) repeat pass interferometry. In the first method, the same SAR system uses two antennas to transmit and receive the signal with a single pass over an area. In the second method, the SAR sensor passes over the same area repeatedly to acquire the interferometric pairs. When the interferometric pair is selected, the interferogram is generated by cross-multiplying, pixel by pixel, the first SAR image with the complex conjugate of the second one (Bamler and Hartl 1998; Rosen et al. 2000).

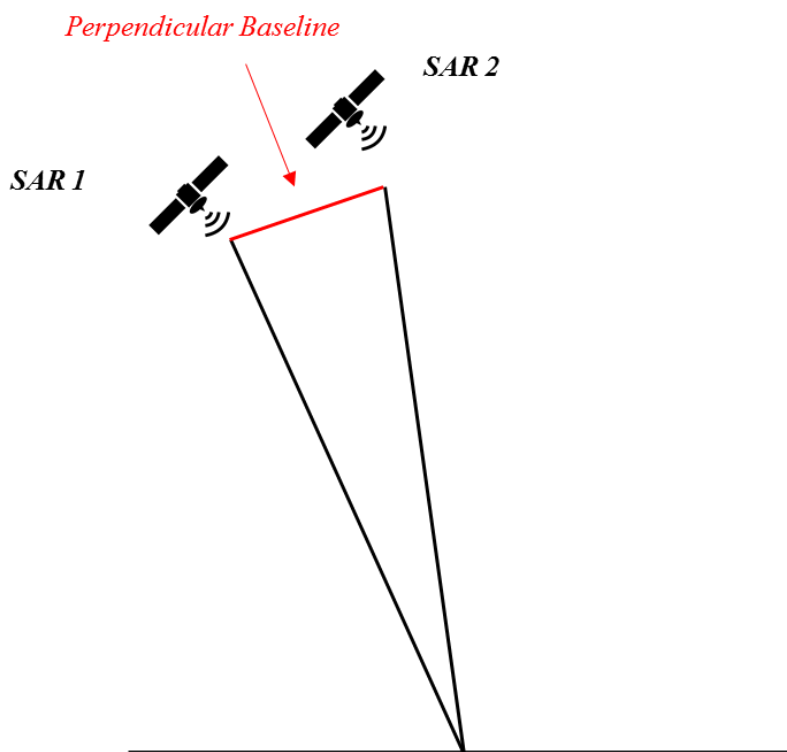


Figure 6 Geometry of a satellite interferometric SAR system

Furthermore, there are some decorrelation factors which affect the interferometric coherence parameter (γ). This term is used to express the measurement of the phase noise and the phase precision (equation 1). Coherence values range between 0 to 1. Higher γ values indicate less noise and consequently more reliable results.

$$\gamma = \frac{\langle s_1 s_2^* \rangle}{\sqrt{\langle s_1 s_1^* \rangle \langle s_2 s_2^* \rangle}} \quad 0 \leq |\gamma| \leq 1 \quad (1)$$

s_1 and s_2 are the two complex images in an interferometric pair
 * signifies a complex conjugate product

Typically, decorrelation sources (equation 2) include:

$$\gamma_{total} = \gamma_{temporal} + \gamma_{geometric} + \gamma_{volume} + \gamma_{thermal} + \gamma_{processor} + \gamma_{DC} \quad (2)$$

- $\gamma_{temporal}$: temporal decorrelation appears when natural changes occur on the targeting objects which can affect the scattering characteristics of their surface.
- $\gamma_{geometric}$: geometric or baseline decorrelation is caused by the difference in the incidence angles between two image acquisitions.
- γ_{volume} : volume decorrelation is produced by the volume of the scatterers. The larger the vertical extent of the scatterers contributing to the radar echo, the greater the decorrelation will be.
- $\gamma_{thermal}$: thermal noise is caused by the system and the antenna characteristics of a sensor.
- $\gamma_{processor}$: processing decorrelation results from the choice of algorithms to perform a number of operation like coregistration or interpolation.
- γ_{DC} : Doppler centroid decorrelation is caused by differences in the Doppler centroids between two acquisitions.

In general, coherent scatterers like man-made structures, bare rocks and soils are preferred for analysis since they can provide reliable results. To minimize decorrelating pixels, users can perform a very accurate coregistration and select interferometric pairs with small temporal and perpendicular baseline.

➤ SAR Differential Interferometry (DInSAR)

Differential Interferometry is an advanced technique which is based on the InSAR method. Though, the term may occasionally be misleading, since InSAR is a differential technique right from the beginning, on DInSAR the subtraction process can be pushed further in other directions (e.g. subtraction of an expected geophysical contribution through earthquake or volcano dynamic modelling). The principle behind differential interferometry is based on the assumption that if the topography is known (e.g. from a DEM), the corresponding phase forming the topography in InSAR (“ Φ_{Topo} ”) can be removed from the interferometric phase (“ $\Delta\Phi_{int}$ ”) and thus

imprinting the deformation on the earth's surface (Ferretti 2007). A visualization of the subtraction between an interferogram and a DEM is depicted in Figure 7 as well as the resulted differential interferogram.

Similarly, DInSAR has the same pros and cons as InSAR and is being affected by the same decorrelation factors and noise that were mentioned above (equation 2). An illustration of the DInSAR technique is depicted in Figure 11 and the basic principles are explained in the next paragraph.

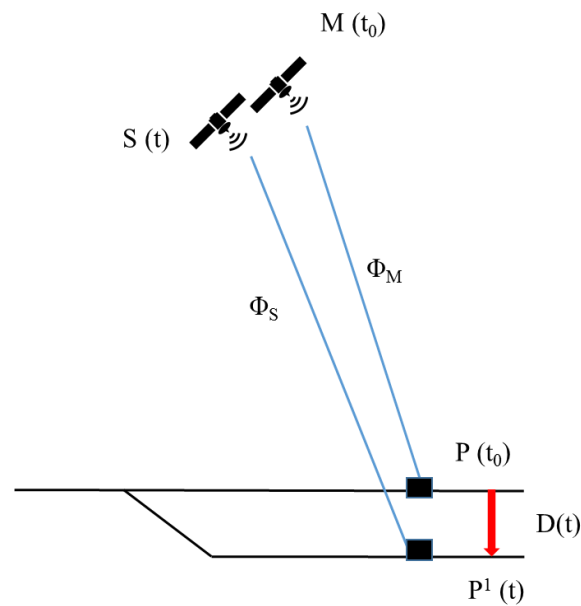


Figure 7 Principle of Differential InSAR for deformation measurement (modified from Crosetto et al. 2005)

The first satellite which is referred as the master (M) acquires the first SAR image at a certain time (t_0) and measures the corresponding phase (Φ_M). If due to an event $D(t)$ that causes crustal deformation, point P moves to P^1 . A second satellite which is usually referred as slave (S) acquires the second SAR image over the same at a certain time (t) and measures the corresponding phase (Φ_S). InSAR techniques exploit the phase difference of Φ_M and Φ_S thus forming the interferometric phase $\Delta\phi_{Int}$. If we assume that the terrain remains stable after the event $D(t)$, point P^1 and P should overlap and the phase difference is connected to the distance difference $SP - MP$, which is the key component for DEM generation using InSAR. In the case where point P moves to P^1 between two SAR scenes, except the topographic phase component Φ_{Topo} , $\Delta\phi_{Int}$ (equation 3) also includes the terrain deformation

contribution $\Delta\Phi_{deformation}$. When a DEM is available, the component Φ_{Topo} can be simulated and subtracted from $\Delta\varphi_{Int}$ and thus, obtaining the DInSAR phase $\Delta\varphi_{D-Int}$.

$$\Delta\varphi_{D-Int} = \Delta\varphi_{Int} - \Delta\varphi_{topo_sim} = \Delta\varphi_{deformation} + \Delta\varphi_{atmosphere} + \Delta\varphi_{noise} + \Delta\varphi_{res_topo} \quad (3)$$

- $\Delta\varphi_{topo}$: The topographic phase component which allows the creation of DEMs or DTMs from InSAR data which it is dependent on the baseline. The larger the baseline, the smaller variations in the topography can be detected.
- $\Delta\varphi_{atmosphere}$: When the two images are acquired at different times, the state of the atmosphere is not identical. Hence, any difference in the troposphere or the ionosphere between the two image acquisitions can change the apparent length of the path between the radar antenna and the ground.
- $\Delta\varphi_{noise}$: Is the phase difference that typically dominated by decorrelation effects which are clarified bellow.
- $\Delta\varphi_{deformation}$: It is the phase that has to isolated from all other phase components in order to calculate the amount of deformation in an area
- $\Delta\varphi_{res_topo}$: Represents the residual component due to errors in the simulation

(Massonnet et al. 1998; Crosetto 2005; Hooper et al. 2012)

3.2 Data

3.2.1 Sentinel 1 - Copernicus Program

After 2012, Copernicus is the new name for the Global Monitoring for Environment and Security program, formerly known as GMES. This initiative led by the European Commission (EC) in cooperation with the European Space Agency (ESA) developing a new family of satellites called Sentinels. These satellites will provide a unique set of observations, starting with the all-weather, day and night radar images from the Sentinel 1.

The radar instrument of Sentinel-1 can operate in four modes: Interferometric Wide Swath (IWS), Extra Wide Swath (EW), Wave (WV) and Stripmap (SM). These

modes can operate in different polarization schemes. The Wave has a single mode polarization (VV or HH). For all other modes, the dual polarization system is available (VV + VH, or HH + HV) as well as single polarization (VV or HH). The interferometric wide swath mode, the default mode over land, has a swath width of 250 km and a ground resolution of 5 x 20 m. This mode images in three sub-swaths using the Terrain Observation with Progressive Scans SAR (TOPSAR).

Global tectonic and volcanic active areas are observed in a stable full two pass IWS mode, VV polarization coverage with a revisit frequency of 24 days per pass (alternating ascending and descending passes, i.e. a particular area is observed every 12 days, interferometric pairs are available every 24 days). Tectonic and volcanic active areas located within Europe are revisited within 12 days per pass in IWS mode, VV-VH polarization.

One of the main applications using IWS mode scenes concerns the monitoring of land deformation. Sentinel 1 beyond being a technological achievement, is the continuation of the previous ESA's radar satellites focusing primarily in the hazard and risk monitoring issues such as volcanoes.

The case of Sentinel-1 interferometric processing (Wegmüller et al. 2015a) presents some peculiarities because of the special TOPSAR mode used by the SAR sensor to acquire the IWS data. The S1 IWS Single Look Complex product (Figure 8), used for interferometric applications, consists of three sub-swaths and each sub-swath image consists of a series of bursts. This image-structure requires geometric and radiometric corrections on a very high standard, so that the generated final mosaic is essentially seamless in both range and azimuth, eliminating the original overlaps between the swaths and the bursts. Other interesting points are that the Sentinel 1 state vectors which are included with the data are very precise, obtaining results in geocoding accuracies less than a few meters even without applying a refinement whereas the orbital tube of the satellite has a narrow width thus obtaining interferometric pairs with small baselines. (Yagüe-Martínez, et al. 2016)

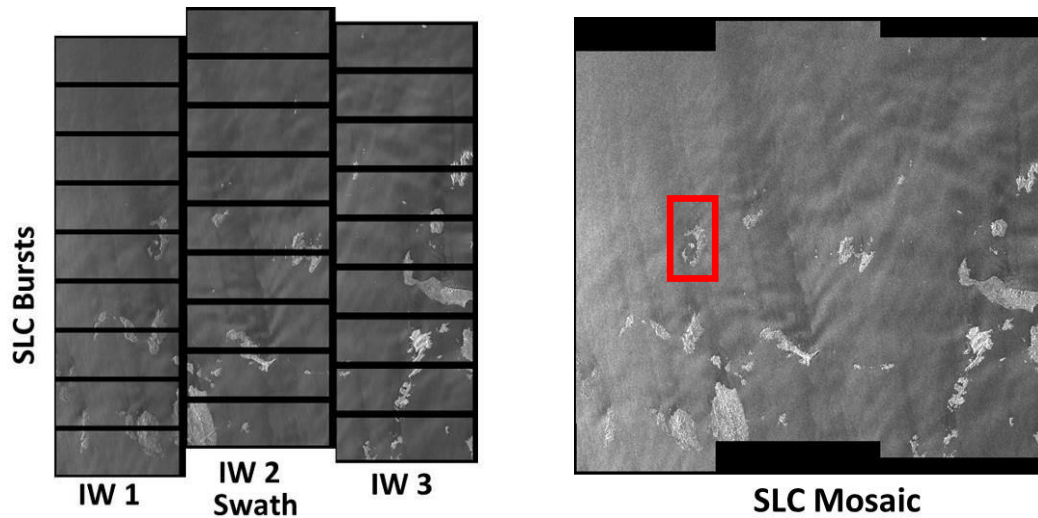


Figure 8 - Sentinel-1A Single Look Complex bursts and sub-swaths (left), SLC mosaic (right)

In this study, two datasets of Single Look Complex (SLC) Sentinel-1A ascending and descending scenes, consisting of 43 and 46 images respectively, covering the period from October 2014 to June 2016 were used to achieve the aim of the project (Table 2). The fact that the volcano exhibits high coherence independently of the temporal baseline allowed for the opportunity to achieve highly reliable results.

Table 2 Sentinel-1A data description.

| Orbit Pass Direction | Acquisition Period | Number of Scenes | Relative orbit number | Incidence angle | Polarization |
|-----------------------------|-------------------------------|-------------------------|------------------------------|------------------------|---------------------|
| Ascending | October 19 th 2014 | 43 | 29 | 34° | VV |
| | June 10 th 2016 | | | | |
| Descending | October 13 th 2014 | 46 | 109 | 36° | VV |
| | June 16 th 2016 | | | | |

3.2.2 Global Positioning System (GPS) Data

GPS is one of the most suitable techniques to measure ground surface deformations because of the high accuracy and provision of the three-dimensional components of the deformation field (East-North-Up). However, the shortage of GPS station density (GPS stations per unit area) is an important limitation of the method. Consequently,

the continuous coverage of interferograms makes the integration of InSAR and GPS a very useful approach to map highly accurate deformations (i.e. at sub-centimetre levels) with unprecedented spatial coverage. Thus, data covering the study period from eleven permanent GPS stations located on the island were obtained to assist the objectives of the project, available from three different data repositories, the two Greek EPOS GSAC repositories and the UNAVCO repository. (Table 3, Figure 9)

Table 3 Coordinates, elevation and length of the obtained observations of the eleven stations.

| Name | UTM34_East (m) | UTM34_North (m) | Elevation (m) | Period of data |
|------|----------------|-----------------|---------------|----------------|
| DSLN | 893390.045 | 4044032.436 | 196.2 | 2014-2015 |
| KERA | 889918.605 | 4039088.470 | 244.6 | 2014-2016 |
| MKMN | 894734.816 | 4038266.259 | 92.9 | 2012-2015 |
| MOZI | 896369.273 | 4043573.679 | 353.7 | 2011-2014 |
| NOMI | 897123.029 | 4039841.657 | 309.7 | 2006-2016 |
| PKMN | 893300.121 | 4036827.952 | 134.4 | 2008-2016 |
| RIBA | 889324.366 | 4043192.837 | 42.0 | 2011-2016 |
| SANT | 896523.213 | 4041141.705 | 392.0 | 2012-2016 |
| SNTR | 891025.028 | 4032442.195 | 137.9 | 2012-2014 |
| THIR | 899453.726 | 4035858.179 | 356.3 | 2012-2015 |
| WNRV | 898018.795 | 4036074.587 | 338.5 | 2012-2015 |



Figure 9 Location of the eleven GPS stations

3.3 Methodology

In the current study two different DInSAR techniques were applied: a) Interferometric Stacking (IS) (Strozzi et al. 2001) and b) Singular Decomposition Value (SVD) or Hybrid Method (Berardino et al. 2002). The principles of each technique will be explained in the latter part of this section. The interferometric processing was carried out using GAMMA Remote Sensing Software. The processing chain on which the whole interferometric processing was based on is presented in detail and illustrated below (Figure 10).

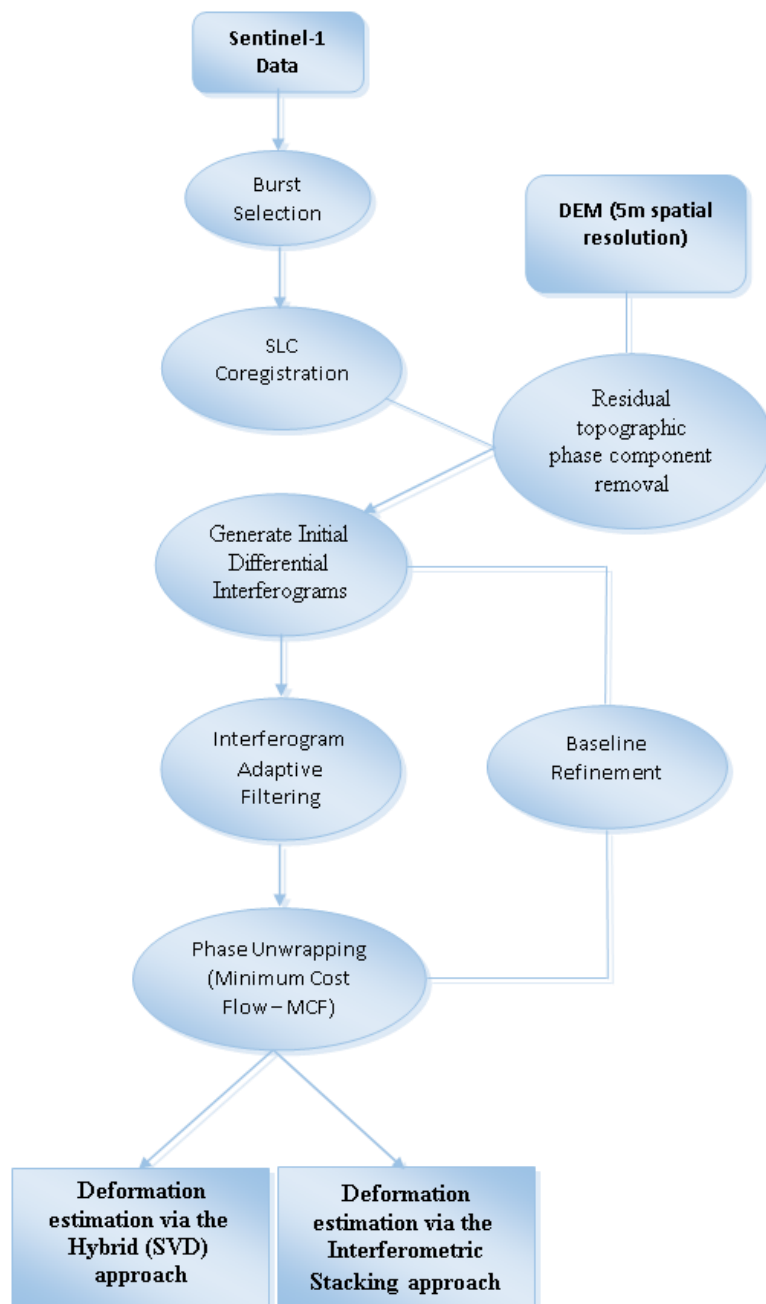


Figure 10 Interferometric processing flow chart.

3.3.1 Processing & Stack Formation

The first step of the processing is to import the raw Sentinel-1A data. An extra step which is not always necessary (depending on the SAR satellite) is the correction of the orbit data which include the instant position and velocity of the satellite. In most cases the state vectors provided with the image data are not precise enough. Even though the orbit data of Sentinel-1 are of high quality, the precise orbit files were obtained in order to eliminate any potential errors that could come up.

By importing the data, radiometric calibration and the mosaicking of the three “Swaths” are also applied in this step and finally, the generation of the Multi-Look Intensity image (MLI) is computed for visualization purposes. The mosaicking procedure combines the three “Swaths” and each of the 9 sub-swath data. The sub-swaths are cut in the overlap region in such a way that only pixels (looks) from the same burst and sub-swath are combined into a MLI pixel (with 10 range looks x*2 azimuth look).

The next step of the processing is to import a Digital Elevation Model (DEM), which in our case is a 5-meter spatial resolution surface model. It is worth mentioning that the DEM is a very important part of the processing chain because it is used in the crucial step of co-registration as well as in the interferogram generation step. The processing strategy of the co-registration of a pair of S1 TOPS SLC is crucial (Prats-Iraola et al. 2015) since interferometry with Sentinel 1 SLC data requires a high quality and precise co-registration of the SLC pairs. Particularly in the azimuth resolution, the accuracy must be a few thousands of a pixel and is absolutely required to overcome the phase jumps (Wegmüller, 2015b). In order to achieve very high co-registration accuracy, the method that is used in GAMMA software, considers the effects of the scene topography from the DEM to determine the refinement of the transformation lookup table. The selected image (master) which was used as basis to coregister the rest of images (slave) was the scene: 20150324 and 20150330 in the ascending and the descending datasets, respectively. Figures 11 and 12 depict the pixel offsets between the master and the slave images that occurred from the coregistration process for the ascending and the descending dataset respectively. Generally, the miss-registration errors are very low and thus are good for an interferometric processing with reliable results.

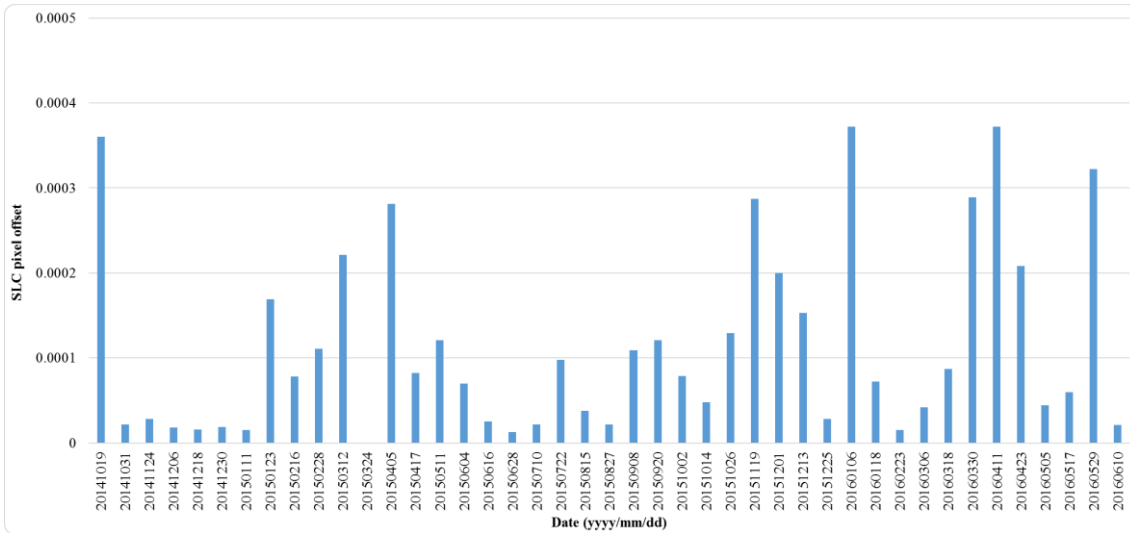


Figure 11 Miss-registration offsets between the master (20150324) and the slave images ascending dataset.

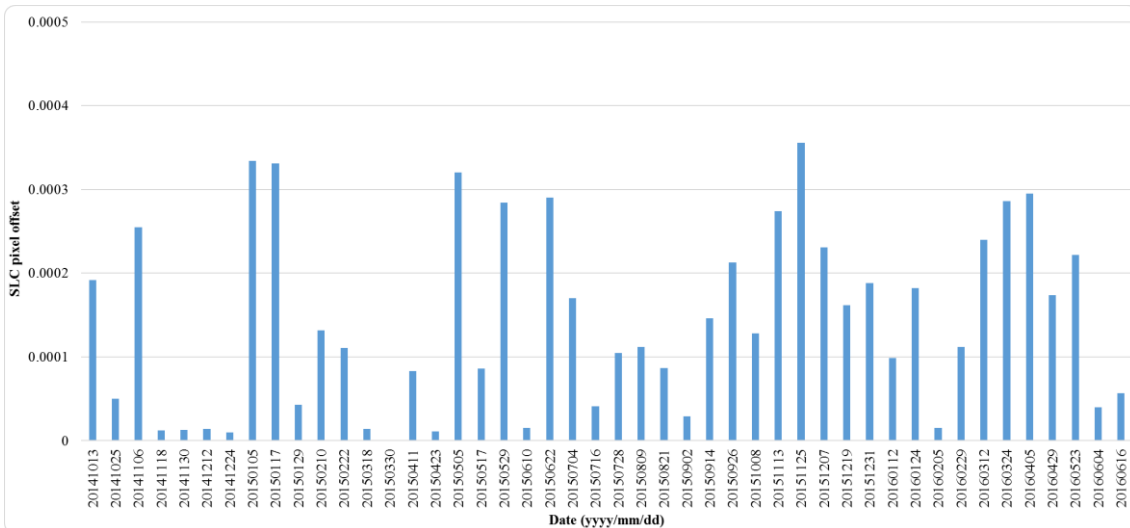


Figure 12 Miss-registration offsets between the master (20150330) and the slave images descending dataset.

Subsequently, the initial differential interferograms were formed, based on two criteria: a) perpendicular baseline, b) temporal baseline. For the first criterion, the maximum allowed baseline value between the interferometric pairs is 200 meters since the study area doesn't include any steep mountainous areas which could lead to extended distortions on the interferograms. Concerning the second criterion, due to the time decorrelation effect on the scenes, the maximum time window selected to form the interferograms is 90 days. Considering those two parameters, 227 ascending and 249 descending interferograms were formed in total, by using a multi-reference

interferogram generation method. Figure 13 depicts the temporal and perpendicular baseline of each combined pair.

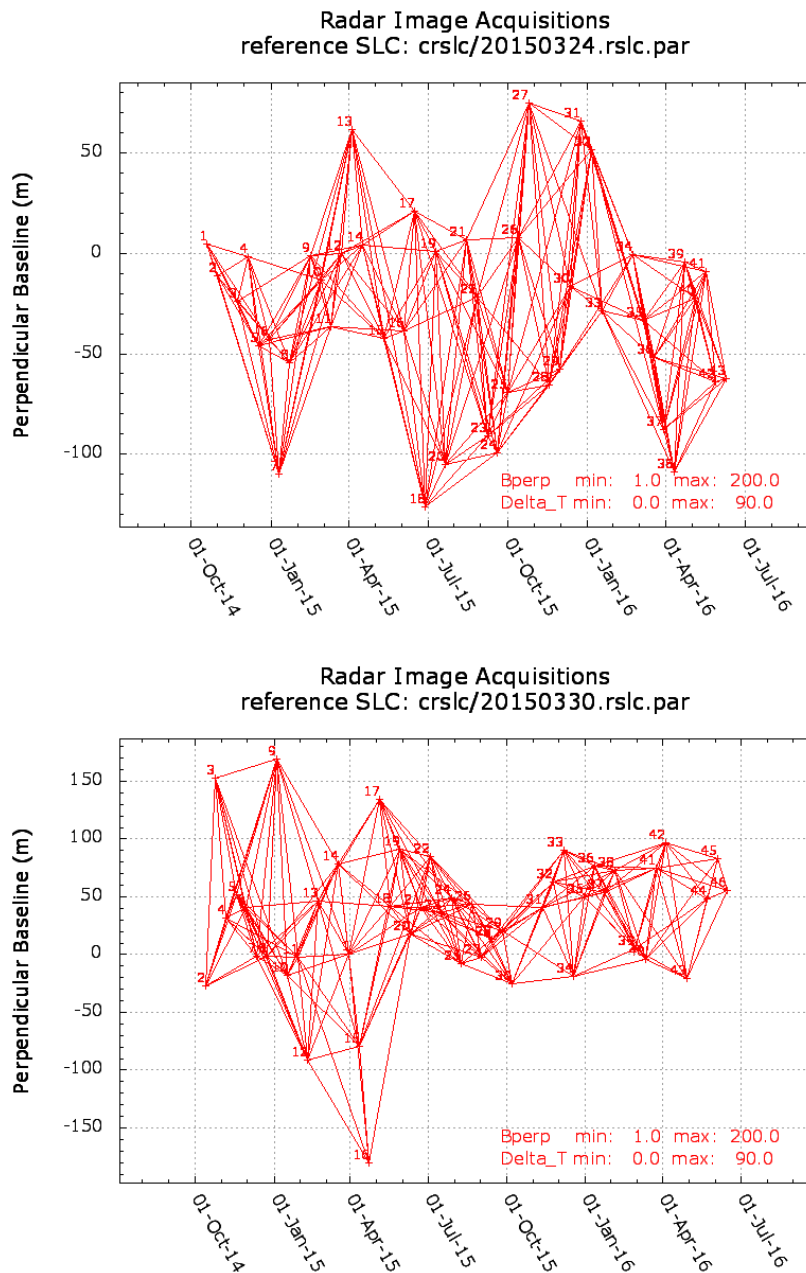


Figure 13 Interferogram network depicting the temporal and the perpendicular baseline of the created interferometric pairs: (up)-ascending, (down)-descending.

Another important result from this step is the generation of the coherence for each interferometric pair. As it can be seen in Figure 14, the average coherence values on the volcano are quite high. Lastly, topography phase parameter was also removed from the differential interferograms using the imported DEM. Next, an adaptive phase

filtering method (Goldstein and Werner 1998) was applied to all differential interferograms, in order to improve the quality of the phase unwrapping step.

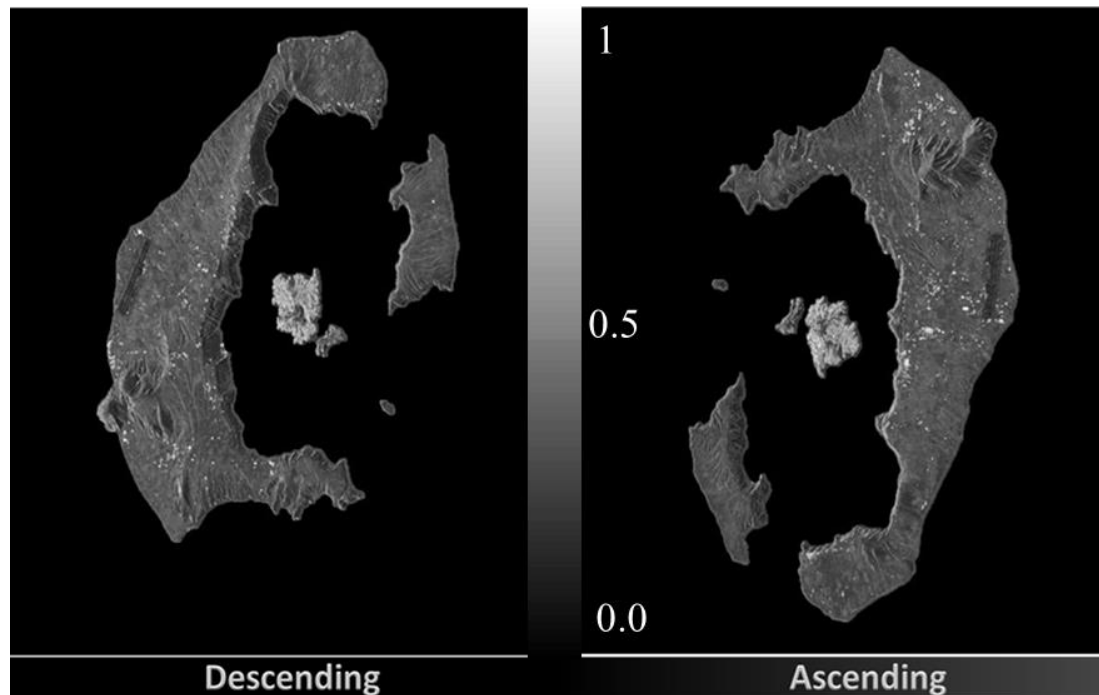


Figure 14 Average coherence images in SAR Geometry.

Concerning the phase unwrapping, the minimum cost flow algorithm (MCF) was applied which was first presented by Costantini (1998). Phase unwrapping is the process of restoring the correct multiple of 2π to each point of the interferometric phase image. The unwrapped phase can be evaluated by a simple path-independent integration of the phase differences of adjacent wrapped phases, starting from a reference location and using the assumption that all phase differences are in the interval $(-\pi, \pi)$. However, in actual interferograms, phase unwrapping is more difficult because of phase steps which are outside of the interval $(-\pi, \pi)$. Causes for local phase gradients larger than π are: i) Phase Noise (temporal decorrelation, shadow and low SNR) ii) Phase Under-sampling iii) Phase Discontinuities (layover and discontinuous surface deformation) (Werner et al. 2002).

After completing the phase unwrapping, in order to achieve better accuracy on the values of perpendicular baseline between all interferometric pairs, a baseline refinement step is required, which re-calculates the initial baselines based on the wrapped and unwrapped differential interferograms already formed. After the execution of the refinement process, the interferograms are re-formed, but this time with updated baseline values for each pair. Additionally, to complete the processing

chain, the phase was converted to displacement with knowledge of the topography from the DEM. Finally, it is important to mention that the differential interferometric phase corresponds to the displacement along the SAR look vector.

3.3.2 Inteferometric Stacking (IS)

The stacking of differential interferograms is based on calculating the average phase of two or more interferograms in a certain time scale in order to reduce the decorrelation factors which cause the phase fluctuations and to extract common information. The most basic procedure of the technique is to compute linear combinations (generally sums or averages) of interferograms. The stacking technique is substantially useful in overcoming shortcomings of conventional InSAR which arise from the negative contribution of two decorrelation factors:

- *Low coherency over long temporal separations:* In the case where reasonable coherency levels cannot be obtained over long time periods, then several short time-period temporally-contiguous interferograms can be summed to produce a pseudo-interferogram over a longer period. This enables low rate displacements to be monitored over longer periods, where no single coherent interferogram exists.
- *Atmospheric influences:* When multiple differential interferograms exist that cover an instantaneous event (such as an earthquake or other sudden ground displacement) they can be summed to increase the (displacement) signal to (atmospheric) noise ratio. Therefore, the resulting stacked interferogram contains mostly the phase which is associated with the deformation phenomenon and less phase connected to decorrelation factors. However, sometimes the only solid way of removing the atmospheric effects is to exclude the affected interferograms from the technique (Zebker and Rosen 1997; Parcharidis et al. 2006; Raucoules et al. 2008).

When applying this method, a reference point on the scene needs to be specified. The reference point works as a point with a phase of zero and based on it, the relative change rate of differential phase for the whole image is calculated. The selection of the location of the point is based on two criteria: a) placing the point on areas with high coherence values and b) placing the point on areas where we already know that

the relative deformation is very low. Usually, the error of the phase rate will increase with incrementing distance from the reference point as the contribution of the phase errors due to atmosphere and baseline error increases. All differential phases are estimated relative to the reference point.

The individual interferogram phases are weighted by the time interval in estimating the phase rate. The underlying assumption is that atmospheric statistics are stationary from one observation to the next. Hence the standard deviation of the phase rate derived from a single interferogram is proportional to $1/\Delta T$ (time interval).

The principle of IS depicts the average linear differential phase change rate (phase rate). The formula below (Equation 4) reflects the differential phase change rate and therefore the displacement rate to all the interferograms for a pixel:

$$ph_rate = \frac{\sum_{j=1}^N \Delta t_j \varphi_j}{\sum_{j=1}^N \Delta t_j^2} \quad (4)$$

The result is a product with the accumulated phase reflecting the average of the phase change rate per year (rad/year). As a final step, the phase rate can be converted to a surface deformation map.

3.3.3 Singular Value Decomposition (SVD)

The second approach involves the implantation of the SVD algorithm in order to obtain the least-squares solution for the phase time-series. This is done by using the multi-reference unwrapped phases that were created in the previous steps. More precisely, the deformation is calculated by using a weighted least-squares algorithm that minimizes the sum of squared weighted residual phases.

Fundamentally, SVD provides a way to calculate an approximate mathematical solution to a singular problem, based on a minimum-norm criterion of the deformation rate to acquire time series (Papageorgiou et al. 2012). The number of singular values (scenes) is equal to the number of times in the output time series.

In practice, SVD algorithm creates single reference stack of deformation rates by using the first scene as master scene with zero deformation values. In this way any potential deformation values that may occur between two dates are added to the subsequent one, for each image acquisition until the last one. Therefore, creating a cumulative deformation history for each pixel that exists in the available time interval and thus enabling the creation of time series graphs. The benefit of this technique is that the non-linear deformation can be estimated without the need of a priori assumption of a deformation model or past knowledge and as any other multi-temporal approach, the mitigation of decorrelation phenomena and topographic inaccuracies are limited (Goel et al. 2011).

Finally, except the produced deformation maps based on the second approach, time series graphs were also produced for specific pixels which overlap the locations of the GPS stations, in order to validate the interferometric results with the ground based geodetic measurements.

4. Results

In this section, the results of the two aforementioned approaches are presented for each SAR geometry (ascending and descending). By transforming the interferometric results from range–Doppler coordinates into map geometry, the interferometric analysis results were imported into a GIS environment for further interpretation and analysis. The deformation maps for the study period (2014-2016) were created using ESRI’s ArcGIS version 10.3.1. Regarding the GPS velocity maps, they were created by Panagiotis Elias (National Observatory of Athens). Finally, the time series graphs, for both line of sight (LOS) SAR geometries, are illustrated for selected locations that overlap the GPS stations in order to derive validated information as well as a GPS-InSAR time series comparison for the GPS station “SANT”.

Figure 15 gives an example of potential motions that InSAR measurements are capable of measuring from the ascending and descending view, respectively.

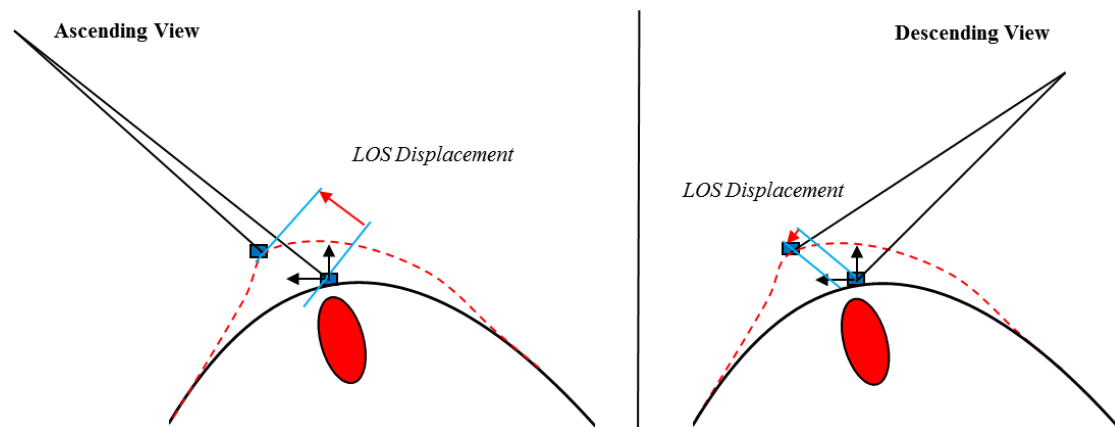


Figure 15 Displacement visible to the line of sight of the ascending and descending views (modified from Bonforte et al. 2011).

4.1 Deformation maps based on the IS method

Using the IS method, two deformation rate maps in LOS direction were created, representing the two different SAR geometries – descending (Figure 16) and ascending (Figure 17) covering the period from October 2014 to June 2016 as a result of stacking 227 ascending and 249 descending differential interferograms, respectively.

The substance (lava) of the volcanic islands presents small time decorrelation effects and thus higher coherence values which lead to more reliable and robust results over the area. Additionally, due to the relatively short time interval of the data (less than two years) and therefore small temporal baseline of the interferograms, it was possible to generate consistent results in other areas where the coherence values are not as high as over N.Kameni.

Results obtained using descending data (Figure 16) show small uplift values of about +3 mm/yr (± 0.6 mm) in the northeast and northwest shores of Nea Kameni, as well as in the center of the island. The rest of the volcanic island seems to have a steady pattern. Moreover, in Palea Kameni there is a uniform displacement of about +3.7 mm/yr (± 0.4 mm) covering the whole extend of the island. Other significant displacement patterns, are located in the north part of the SVC, close to the Kolumbo fault line (+5-7 mm/yr), as well as in southeast part of Thirassia.

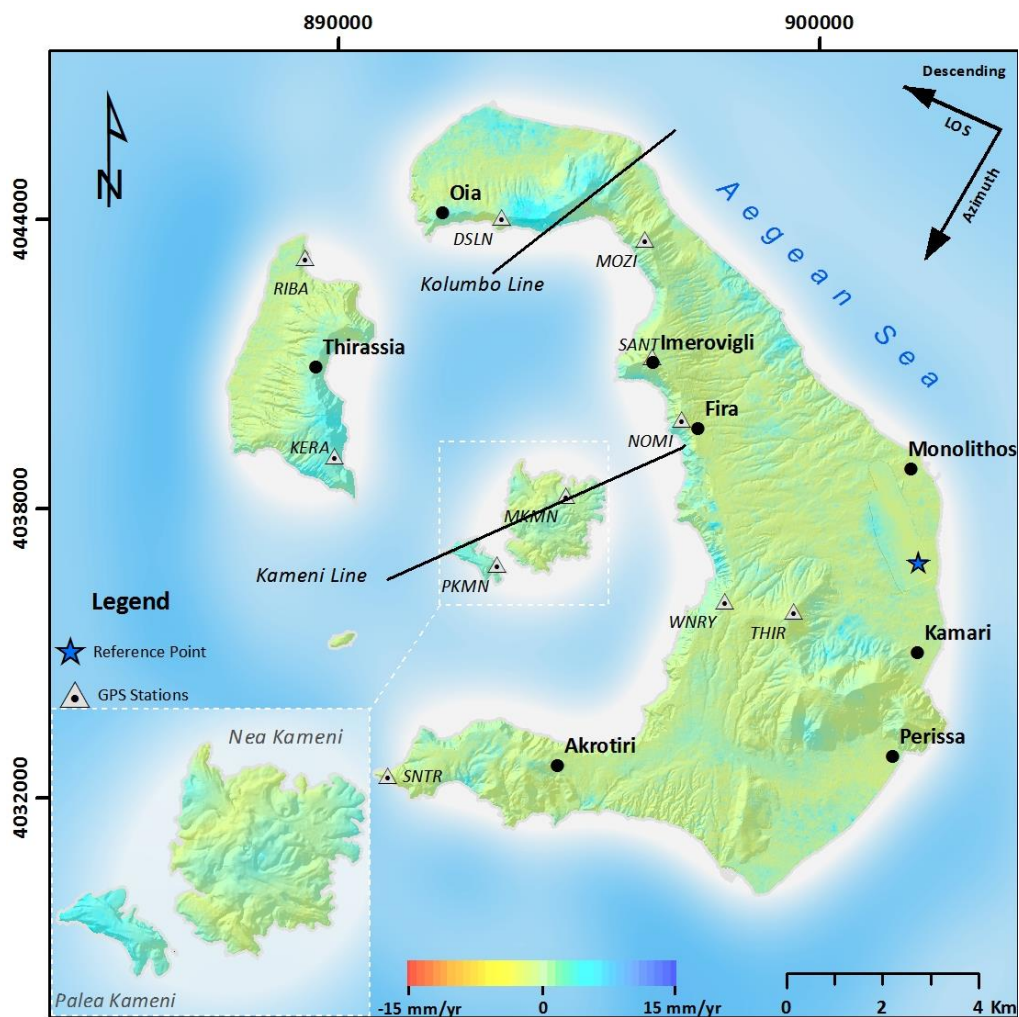


Figure 16 Average LOS (descending) deformation over Santorini for the period October 2014- June 2016.

Results derived from ascending data (Figure 17) present small similarities with the descending results. In particular, higher rates of uplift can be detected all over Nea Kameni, around 10.5 mm/yr (± 1 mm) at the west-center part and 7.5 mm/yr (± 0.4) at the east part. However, similar patterns can be observed in Palea Kameni whereas the rate is higher (5 mm/yr) the deformation form is the same. Likewise, the southeast part of Thirassia is presenting uplift rates of about 6-8 mm/yr. Furthermore, the deformation spotted along the Kolumbo line in Figure 16 is absent in the ascending results indicating a potential horizontal motion of the ground.

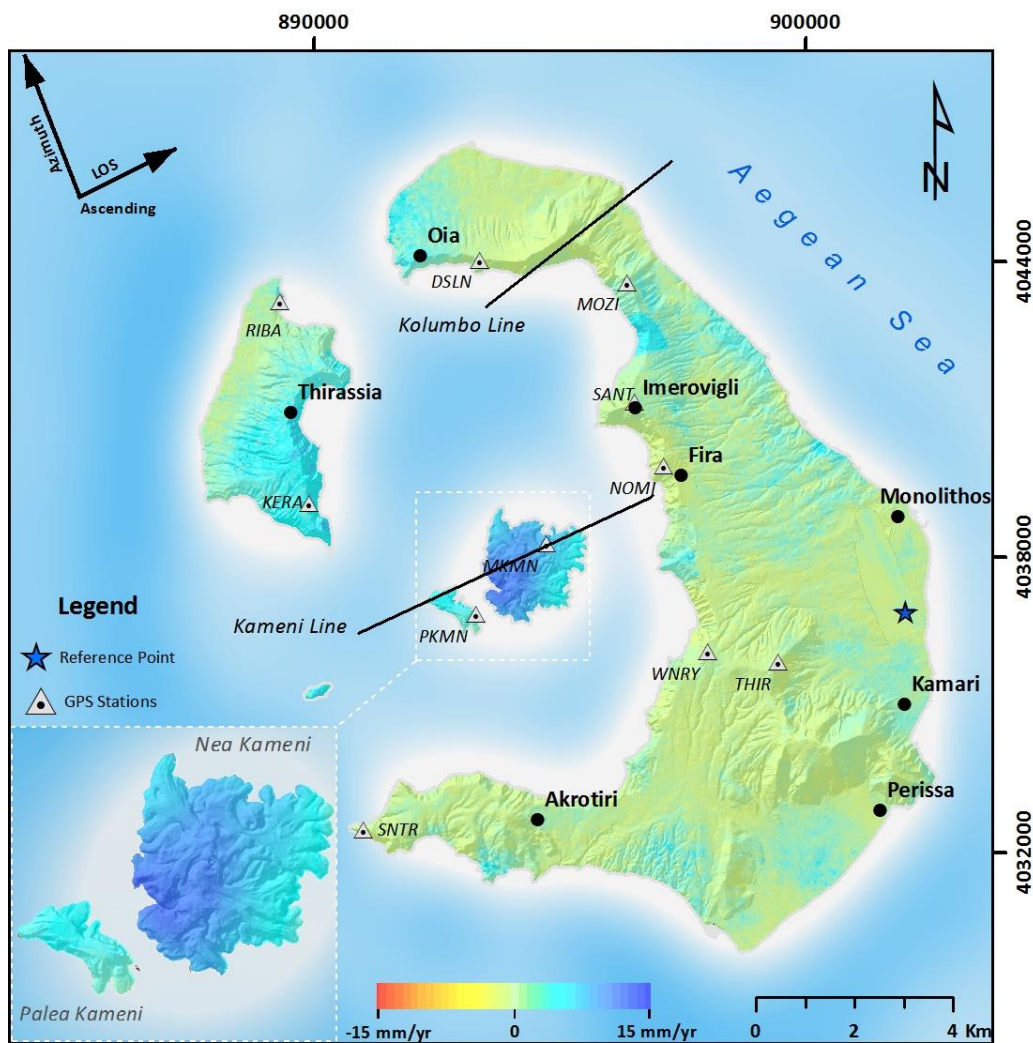


Figure 17 Average LOS (ascending) deformation over Santorini for the period October 2014- June 2016.

4.2 Deformation maps based on the SVD method

In a similar fashion, by applying the SVD method, two deformation maps were created using the same number of differential interferograms for the corresponding period.

Firstly, the results attained from the descending dataset (Figure 18) illustrate a smoother but analogous to the IS method deformation pattern. The centre of Nea Kameni, displays a rate of +2.5 mm/yr (± 0.3 mm), slightly smaller compared to the results from the IS method, while Palea Kameni has slightly higher rate of about +5.7 mm/yr (± 0.4 mm). Similar rates can be found at Thiriassia island, while the displacement pattern located along the Kolumbo line is almost absent in this method, apart from some low uplifting rates east of “DSLN” station.

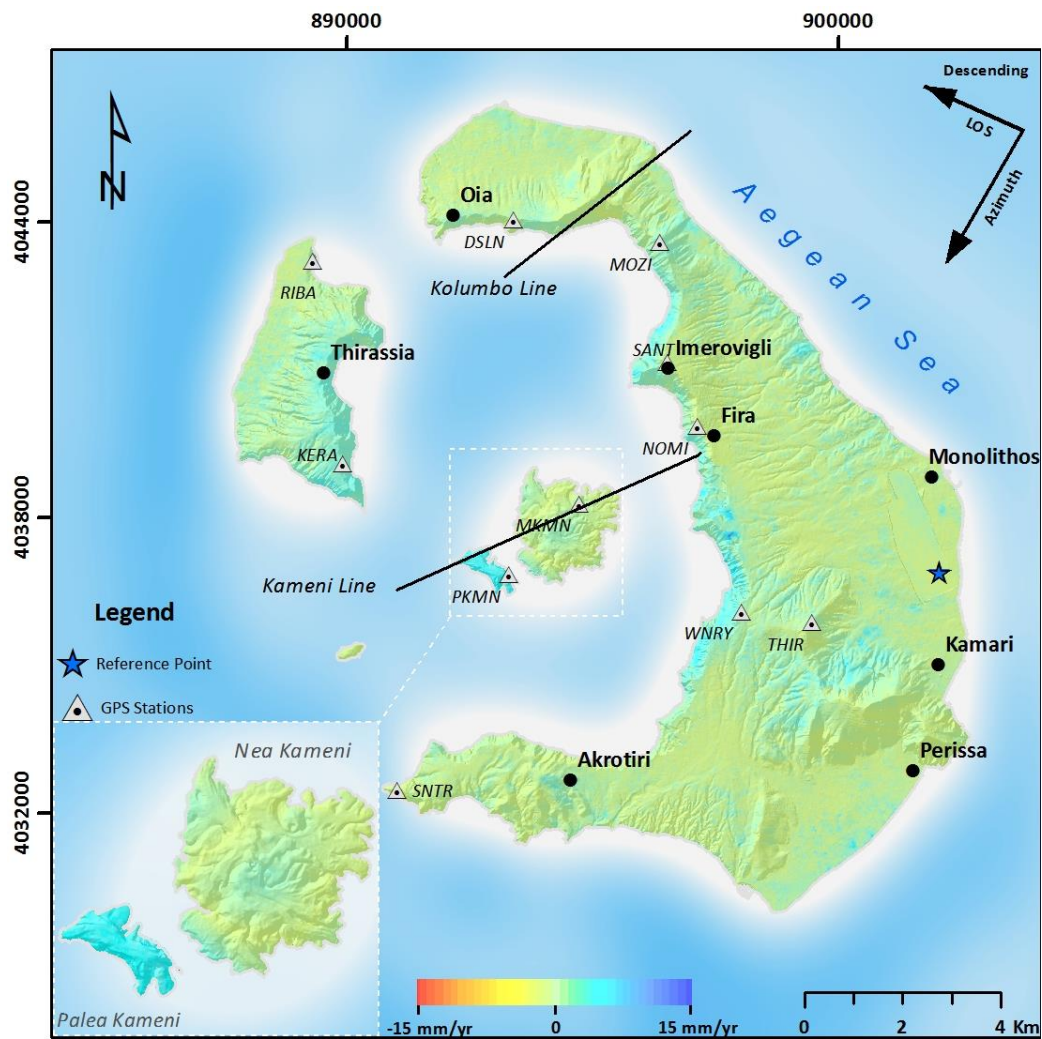


Figure 18 Average LOS (descending) deformation over Santorini for the period October 2014- June 2016.

Concerning the ascending SVD case (Figure 19), it is clear that the deformation pattern is almost identical to ascending IS case, but with higher rates. This is more evident at Nea Kameni, where the rate peaks at around 12.5 mm/yr (± 0.8 mm/yr) and is situated mostly at the central and southwestern parts indicating in this way a horizontal motion. Palea Kameni steadily displays signs of uplift in agreement with other geometries and methods, reaching rates of about 7.1 mm/yr (± 0.5 mm/yr), as well as in Thirassia island, where the same pattern can be recognized with uplifting rates of about 7.0-8.5 mm/yr.

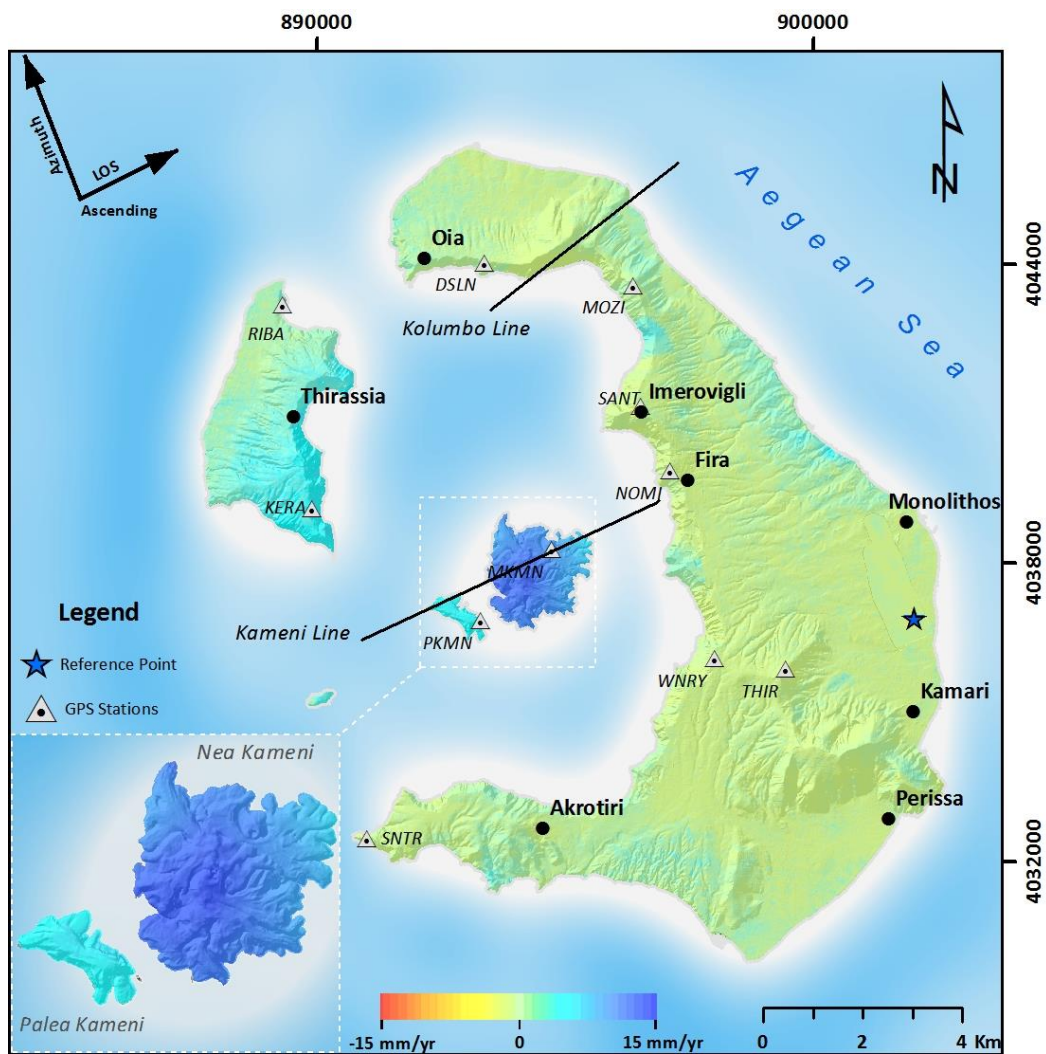


Figure 19 Average LOS (ascending) deformation over Santorini for the period October 2014- June 2016.

4.3 GPS velocity maps

In this study, GPS maps were acquired and have a complementary role in order to have a second assessment of the vertical but most importantly, the horizontal motion, which takes place at the SVC and it is more difficult to be measured with InSAR techniques. Generally, the GPS measurements (Figure 20 & Figure 21) display a diverse displacement pattern in comparison to the SAR-based results. More specifically, Nea Kameni displays low subsiding values but also a northwest motion while Palea Kameni shows a north-east motion along with a minimal vertical velocity. Further noteworthy horizontal motions can be spotted close to Oia, at station “DSLN” and to stations “MOZI” and “THIR”. Moreover, high positive vertical rates can be detected in most stations and especially in “WNRV” and “THIR”, where the rate reaches 6.2 mm and 4.4 mm, respectively.

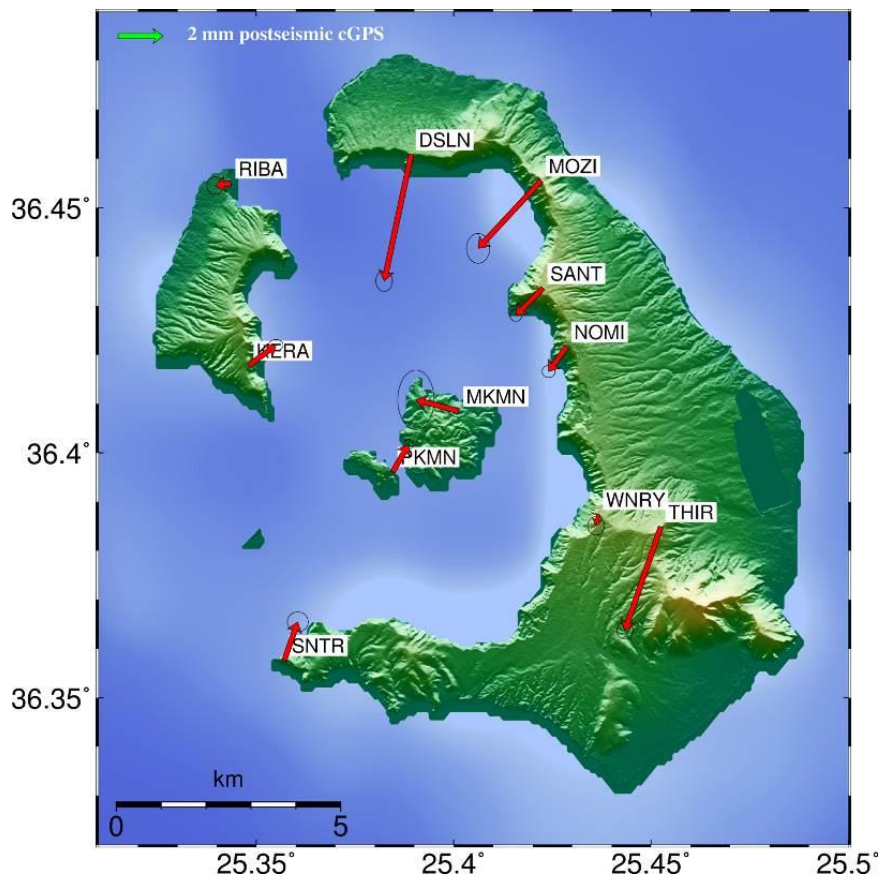


Figure 20 Horizontal GPS ground velocity map for the post-unrest period (source: National Observatory of Athens, P. Elias)

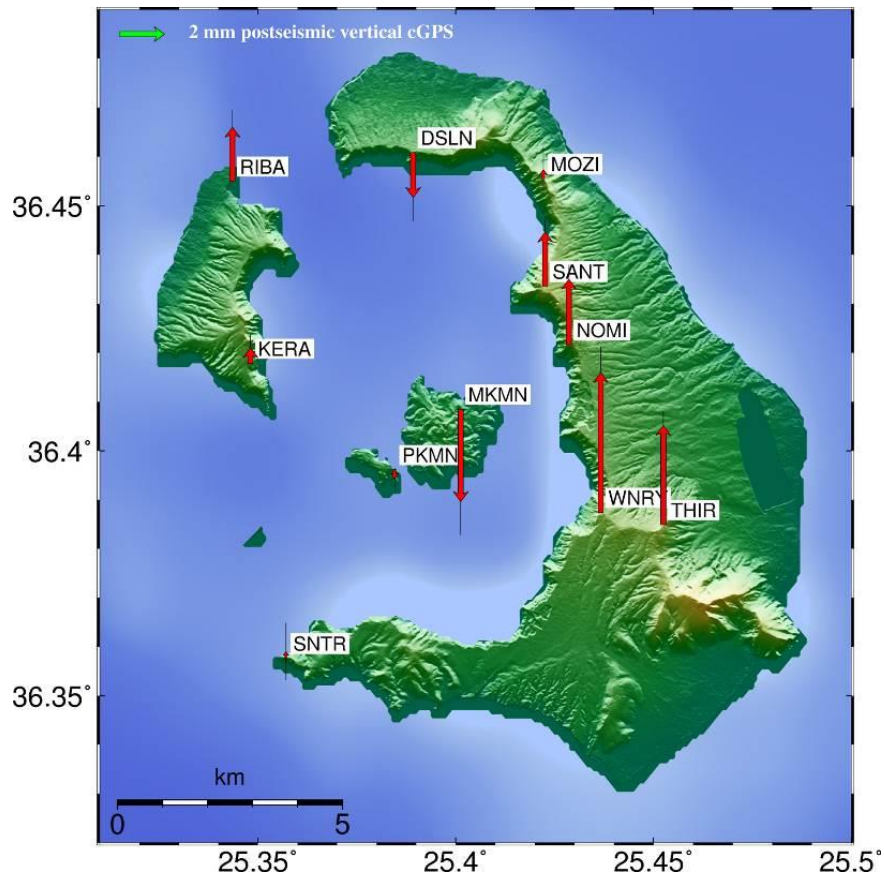


Figure 21 Vertical (right) GPS ground velocity map for the post-unrest period (source: National Observatory of Athens, P. Elias)

Table 4 Mean annual velocities based on GPS measurements for east, north and vertical components.

| Name | East | | North | | Up | |
|------|------------------|-----------------|------------------|-----------------|------------------|-----------------|
| | Velocity (mm/yr) | Sigma (\pm) | Velocity (mm/yr) | Sigma (\pm) | Velocity (mm/yr) | Sigma (\pm) |
| DSLN | 5.7 | 0.2 | -21.1 | 0.3 | -2.0 | 0.6 |
| KERA | 8.1 | 0.2 | -14.6 | 0.2 | 0.7 | 0.3 |
| MKMN | 5.0 | 0.5 | -15.0 | 0.8 | -4.1 | 0.9 |
| MOZI | 4.1 | 0.3 | -18.5 | 0.4 | 0.4 | 0.6 |
| NOMI | 6.1 | 0.2 | -16.6 | 0.2 | 2.9 | 0.4 |
| PKMN | 7.6 | 0.1 | -14.3 | 0.1 | -0.4 | 0.3 |
| RIBA | 6.2 | 0.2 | -15.6 | 0.2 | 2.4 | 0.5 |
| SANT | 5.7 | 0.2 | -16.7 | 0.2 | 2.4 | 0.3 |
| SNTR | 7.5 | 0.3 | -13.8 | 0.3 | 0.3 | 0.8 |
| THIR | 5.3 | 0.2 | -20.1 | 0.2 | 4.4 | 0.4 |
| WNRV | 6.8 | 0.2 | -16.0 | 0.3 | 6.2 | 0.7 |

4.4 InSAR Time Series

Using the SVD method time series, charts were created in order to monitor the displacement through time for designated pixels which are situated on the geographical coordinates of the GPS stations. Particularly, 6 GPS stations were selected (DLSN, KERA, MKMN, THIR, SANT, PKMN) which are plotted in Figure 22 and Figure 23, representing the descending and ascending cases, respectively.

Beginning with Nea Kameni time series in Figure 22, point (MKMN) presents a stable course with minimal fluctuations throughout the whole study period. However, a noteworthy linear deformation pattern can be observed at Palea Kameni (PKMN) which steadily increases with time.

On the other hand, the rate of change for points located at “KERA” and “THIR” is inversely associated. Continuing, point “SANT” which is located at Imerovigli, depicts a deformation pattern which tends to repeat approximately every 6 to 7 months, starting every winter (December-January) and finishing in the beginning of summer (May-June). Finally, point “DLSN” (east of Oia), shows an indistinct course with low displacement rates.

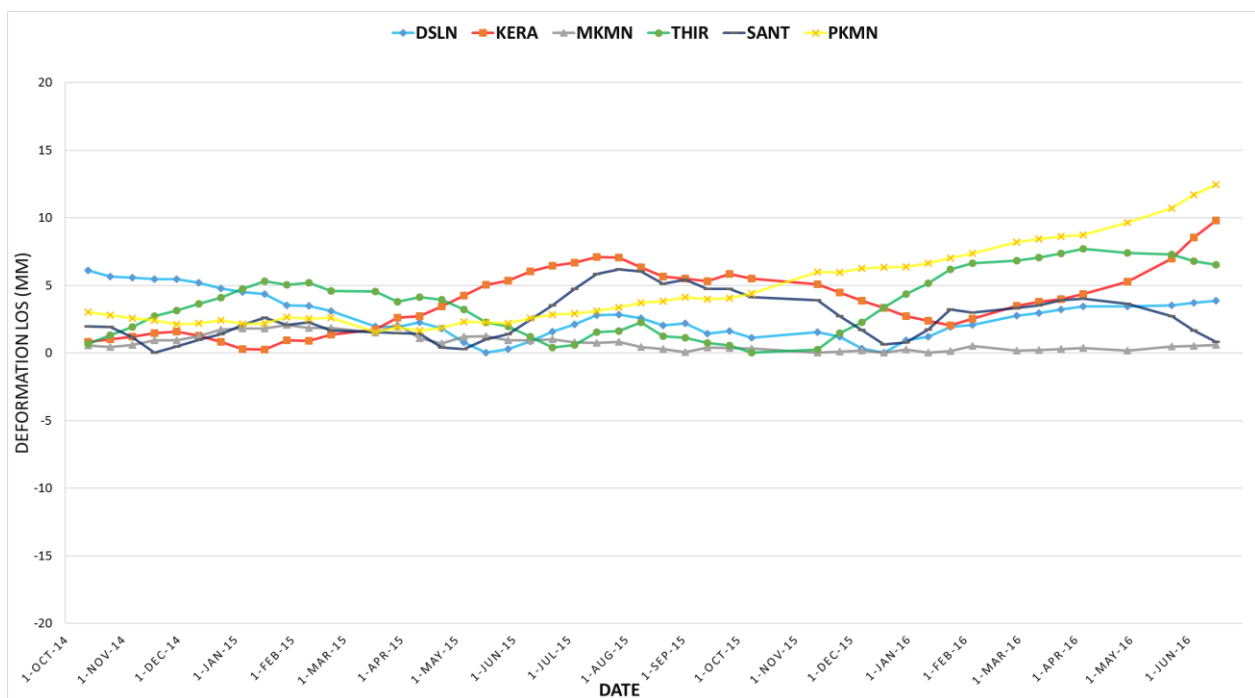


Figure 22 InSAR Time Series LOS (Descending) displacement measured on the geographical coordinates of six GPS stations.

Most points, following April of 2015, depict a very diverse pattern through the remaining study period. Prior to this date most points show a steadier pattern with relatively low rates of deformation.

The LOS deformation rates depicted in the ascending time series graph (Figure 23) have small similarity in comparison to the descending one. However, the same remark about the discrepancy of the deformation rates after April 2015 which was observed in the descending graph can be seen in the ascending one as well. More specifically, Nea Kameni (MKMN) illustrates quite high LOS uplifting values which increase through time, while Palea Kameni (PKMN) shows the same strong linear deformation pattern that can be observed in Figure 22. Concerning the point “KERA”, which is located at Thirassia island, a gradual increase after the summer of 2015 that peaked around March 2016 can be seen, whereas, a slow but steady decrease of the signal is detected since then. The rest of the point-stations (DSLNL, THIR and SANT) depict a close pattern which presents no repetition through time with rates less than 5mm/yr. Finally, they illustrate small resemblance in the behavior through time in comparison to the equivalent descending time series rates.

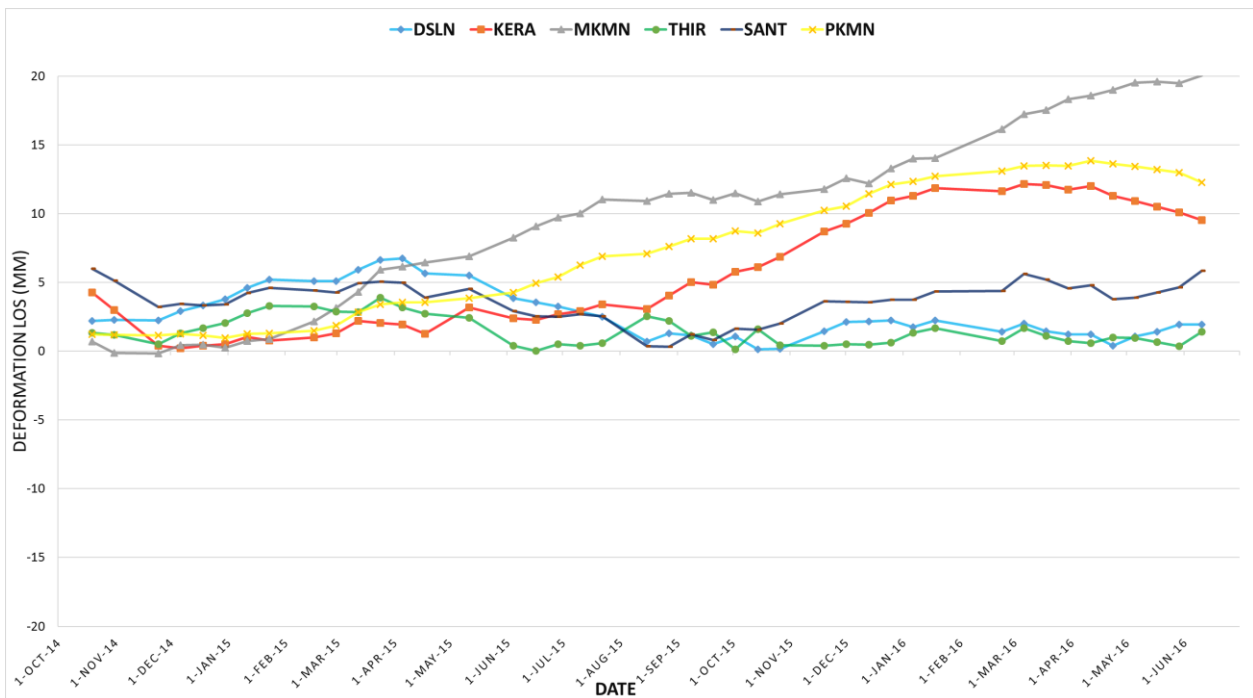


Figure 23 InSAR Time Series LOS (Ascending) displacement measured on the geographical coordinates of six GPS stations.

4.5 InSAR & GPS Time Series comparison

In order to have a closer view and a more detailed comparison of the InSAR time series with the GPS measurements, a time series graph was also obtained for the only available station (“SANT”). Thus, the equivalent InSAR time series graph was created containing both ascending and descending data for the mentioned station.

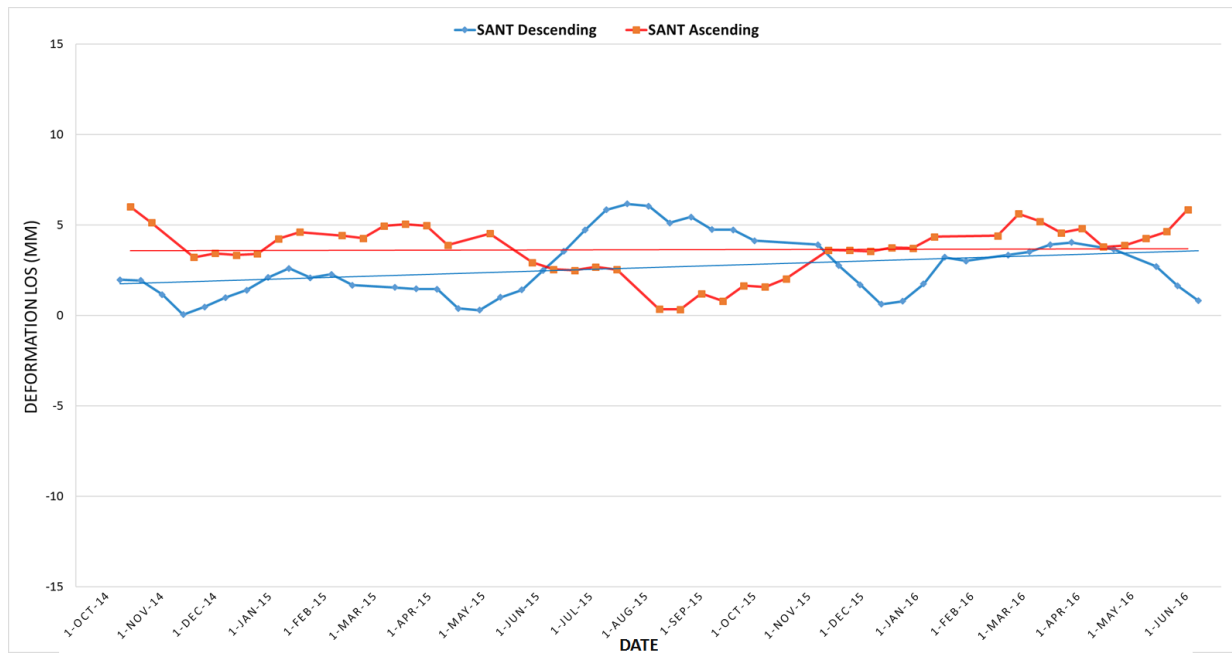


Figure 24 InSAR Time Series LOS (ascending and descending) displacement measured on the geographic coordinates of the GPS station “SANT”.

Reviewing station “SANT” time series graph (Figure 24), a small but steady positive inclination can be observed from the trend line and the average deformation rate is estimated around +3.5-4mm/yr at the time of the last acquisition (June 2016). By comparing the mentioned facts with GPS time series as depicted in Figure 25, InSAR results can be confirmed by the GPS measurements which estimate the average vertical deformation rate at the same range (+3.5–4 mm/yr).

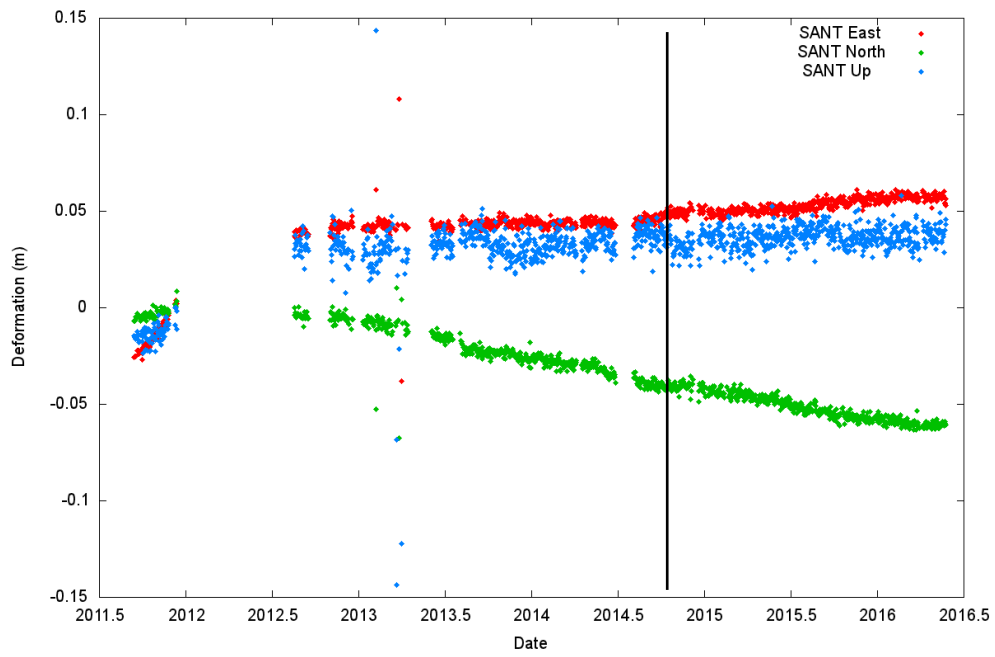


Figure 25 GPS time series depicting the ground velocities on station “SANT”. (National Observatory of Athens, P.Elias)

5. Discussion-Interpretation

InSAR results unveiled that a probable but significant horizontal motion is taking place over Nea Kameni island which can be partly confirmed by the horizontal GPS ground velocity map. High positive rates appear in the ascending geometry while small positive rates or even zero appear in the descending one. On the other hand, Palea Kameni displays a less complicated motion, both geometries present signs of ground uplift around 5.5-6.5 mm per year and thus assuming a vertical motion is taking place. Thirassia island has similar deformation characteristics with Nea Kameni, although coherence values are lower especially on the north-west part of the island, resulting in less reliable results. However, GPS measurements complicate the interpretation of the detected movements over the SVC. That can be contributed to two reasons; a) shorter period of data in comparison to SAR data and b) due to the differences in the sensitivity to detect deformation along certain directions, such as a N-S motion, between the InSAR and the GPS measurements. Conceivably, the measurements from GPS and InSAR over N. Kameni imply a northwest motion which is apparent from the ascending deformation map and the GPS station on the volcanic island. The low subsidence rates that GPS data present over N.Kameni are not confirmed by the InSAR results which display low inflation or zero displacement rates, possibly due to the influence of the stronger horizontal motion that was mentioned before.

To interpret the results that were obtained for this deformation pattern, seismic events data were collected from the Institute of Geodynamics of National Observatory of Athens, covering the period of October 2014 to June 2016 (Figure 26). Further comparison with seismic data reveal that the diverse displacement pattern which was observed in both InSAR time series graphs can be potentially associated with the significant decrease of seismic activity in the area around April of 2015. In fact, during the period between October 2014 to April 2015 more than the half (32) of the seismic events that occurred in the area are contained, while 31 took place for the remaining period (14 months). Hence, there is a strong indication which supports the hypothesis of a correlation between the seismicity and the sudden deformation pattern alteration in the area. Additionally, judging by the timeline of the seismic events, it is reasonable to presume that the seismicity in the area is slowly decreasing in time.

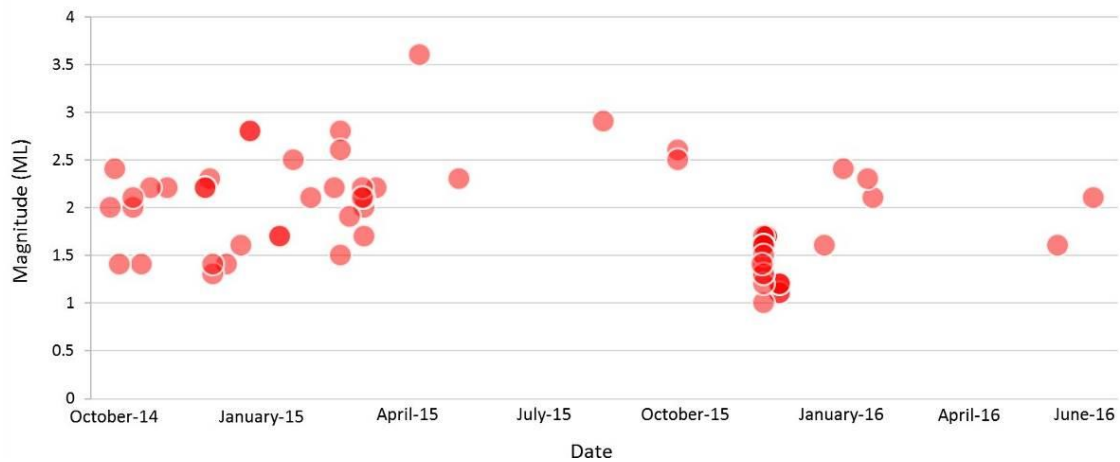


Figure 26 Plot depicting the local seismic events during the study period October 2014 to June 2016 (source: National Observatory of Athens).

It is evident that Santorini volcano has entered a new period of activity. After the obvious signs of unrest, the general pattern over Santorini seems to stabilize and present new features. As seen from the results, SVC is currently characterized of further decrease of seismicity in the area and low deformation rates that are located over the two volcanic islands and Thirassia. Thus, it is reasonable to assume that the detected displacements pose no imminent threat to buildings, the road network or any other man-made structures that could cause damage to the island's proper functionality or to the local population.

Moreover, it is important to mention that the interferometric results present some limitations mostly at the caldera walls which include vastly steep slopes of approximately 300 meters high and thus, hindering the estimation of the deformation that occurs, from both ascending and descending data, since many areas are not visible to the LOS of the SAR sensor in both geometries. Several areas (such as north-east from Imerovigli) present irregular and unreasonable displacement surfaces. This can be contributed to two possible reasons: a) atmospheric effects or b) low coherence values which cause unreliable and unrealistic results.

Generally, the results based on the IS method are closer to the GPS measurements comparing to the SVD ones, which however present a smoother surface of deformation rates as depicted in the produced maps. A concise appraisal and comparison between the two DInSAR methods over Nea Kameni is illustrated in the

following figures. More specifically, two topographic profiles A-B (figure 27) and C-D (figure 28) were formed representing the elevation across the lines with their corresponding deformation estimation, including both acquisition geometries.

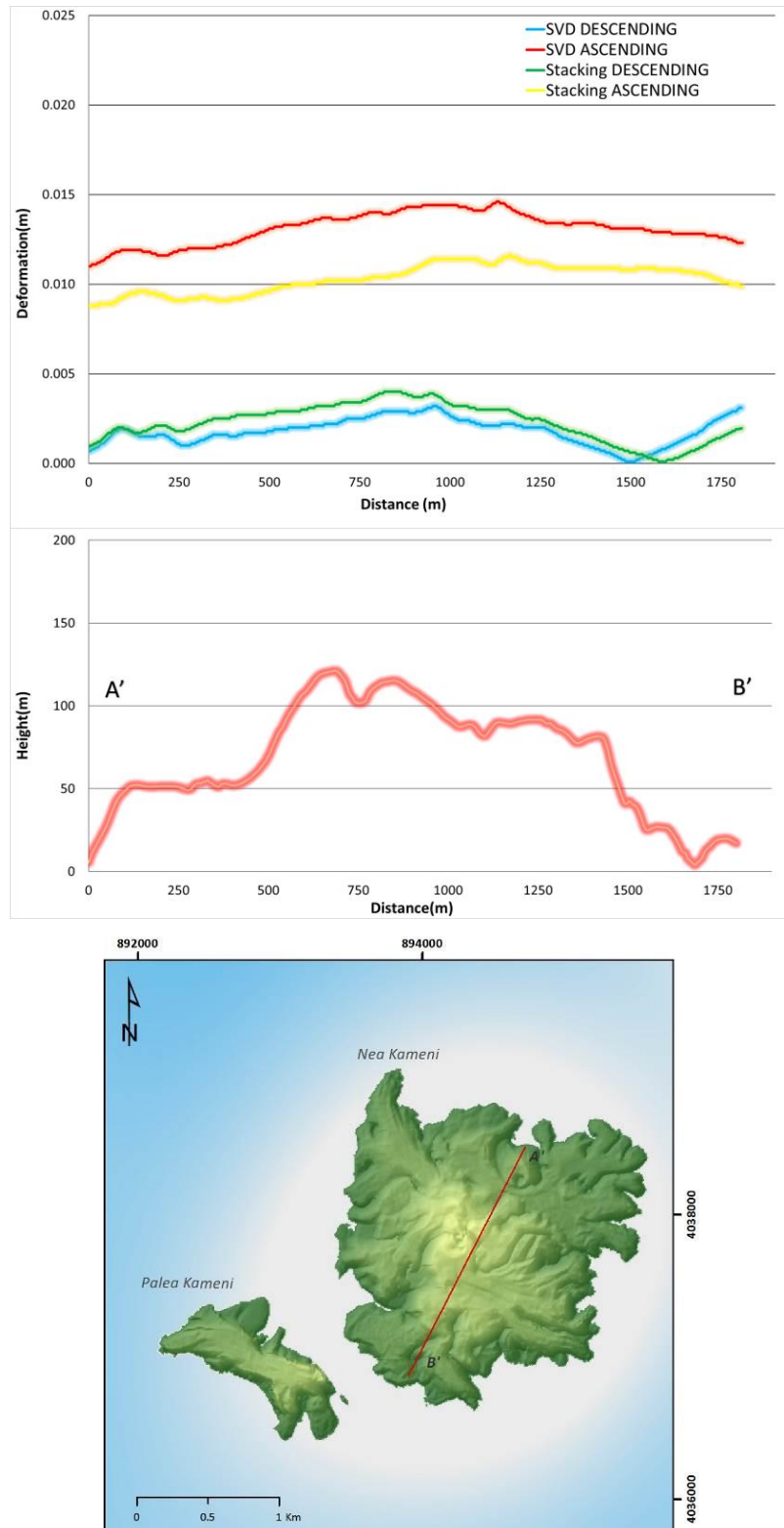


Figure 27 2-Dimensional deformation profile (A-B) over Nea Kameni and their corresponding elevation profiles.

In general, both methods clearly produced similar results and especially on the descending geometry where even the highest discrepancy is lower than 1mm and there are also cases where the deformation rates are almost identical, especially in the C-D profile.

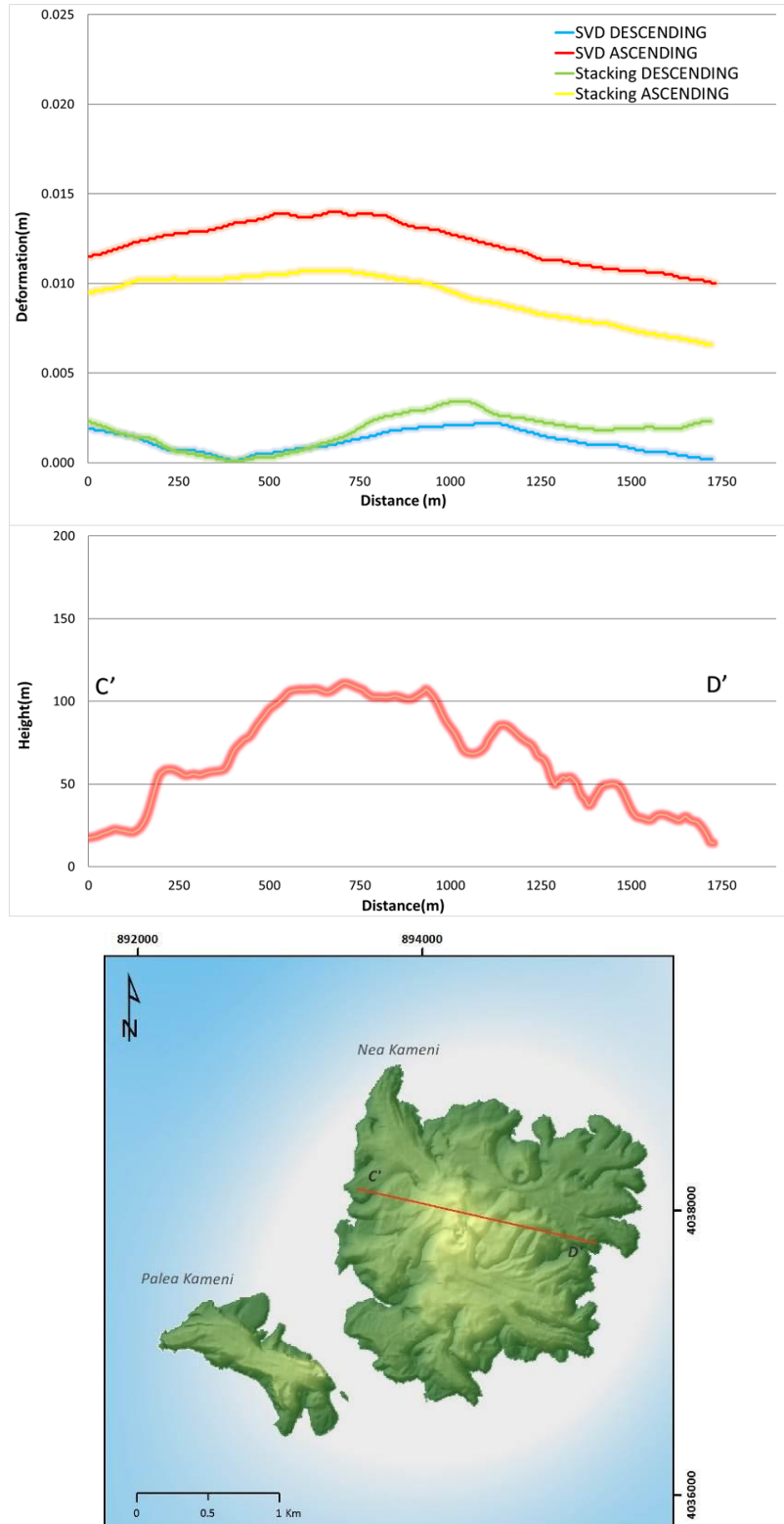


Figure 28 2-Dimensional deformation profile (C-D) over Nea Kameni and their corresponding elevation profiles

Evidently, in the ascending geometry the deviations are higher but in a very parallel way, since the displacements rates display a constant 4mm difference with slight or no variations through the extent of the profile. An overall remark is that the descending case presents smoother results in comparison to the ascending one, which however, is not the case when comparing the two methods, since there is no solid indication that one produces smoother or rougher results than the other one. Additionally, fluctuations in the deformation rates appear between the two methods where steep terrain is found, as for example in profile A-B (around 1500 meters distance), which is anticipated since steep topography causes bigger geometrical distortions in SAR images.

Sentinel-1A data revealed several important scientific characteristics that can influence future research in the field of environmental risk monitoring. Particularly, monitoring applications which require frequent observation and measurements will be much easier to conduct. This is due to the possibility of obtaining satellite images in less than 24 hours after their acquisition, every 12 days for Sentinel-1A data and even less with the combination of Sentinel-1B (6 days revisit time). This high temporal resolution is an exceptional asset that can be utilized for monitoring applications like volcanoes, critical structures, floods, earthquakes and other natural hazards that require continuous or periodic observation. Moreover, the data sets are available for the whole scientific community with no limitations, eradicating obstacles that are related to financial difficulties and of course, making research prospects simpler.

Finally, future studies should be conducted over a longer period by utilizing Sentinel 1 data in order to have a better understanding and knowledge of the displacement pattern, since the availability of the Sentinel-1 archive is short in length. Inevitably, the study period in the present thesis is relatively small (less than two years) but is a first step towards examining the performance of Sentinel 1 for environmental monitoring through InSAR methods. More complicated, but also more robust techniques such as the Persistent Scatterers Interferometry (Ferreti et al. 2000) could be applied, which could lead to results with smaller atmospheric effects and more precise and accurate estimations of the ground displacement. Finally, GPS data with increased station density and expanding over a larger period, would pose as a valuable asset in improving the evaluation and comparison of InSAR results and thus, offering a more robust overview of the underlying processes that are taking place in SVC.

6. Conclusions

In the current study, Sentinel-1A descending and ascending data were used for the first time to evaluate the deformation pattern in Santorini Volcanic Complex (SVC), an immensely active area, and particularly on Nea Kameni island.

Initially, the potential of two DInSAR techniques (Interferometric Stacking and Singular Value Decomposition) was demonstrated and the analysis of Sentinel-1A data succeeded to estimate the deformation pattern. Both methods produced similar results, especially in the descending geometry where the results were almost identical, while in the ascending geometry the deviations between the two methods were higher. The produced deformation maps and time-series graphs depict important characteristics for the SVC activity. More specifically, InSAR results revealed a significant horizontal motion that is taking place over Nea Kameni and low uplifting rates over Palea Kameni. Time series analysis displayed a clear linear trend in Palea Kameni and an interesting deformation pattern that repeats through time in several areas. Additionally, interferometric time series revealed a potential association between the decrease of seismicity and the alteration of the deformation pattern which was detected in both acquisition geometries around April 2015. However, GPS measurements are not in full accordance with InSAR results, possibly due to the shorter availability of the GPS data and due to differences in the sensitivity to detect deformation along certain directions, such as a horizontal motion which is more difficult to measure with InSAR. It is evident in the present study that Santorini Volcanic Complex has entered a new stage that has different characteristics from the beginning of the post-unrest period. The current period is defined by a vertical and uplifting motion of Thirassia and the volcanic islands (Nea and Palea Kameni) in contrast to Santorini which presents a stable pattern and further decrease of the seismic activity in the area and nearly absent inside the caldera walls.

Sentinel-1 data demonstrated new possibilities for monitoring applications, which require continuous observation and measurements such as volcanoes, critical structures, floods, earthquakes and other natural hazards. Undeniably, the Copernicus program offers fast, easy to access and unrestricted data to the public enabling in this way, studies like the one conducted feasible, by minimizing expenses and resolving problems that arise from having access to data.

7. References

- Amelung, F., Jónsson, S., Zebker, H. and Segall, P., 2000. Widespread uplift and 'trapdoor' faulting on Galapagos volcanoes observed with radar interferometry. *Nature*, 407(6807), pp.993-996.
- Antonielli, B., Monserrat, O., Bonini, M., Righini, G., Sani, F., Luzi, G., Feyzullayev, A.A. and Aliyev, C.S., 2014. Pre-eruptive ground deformation of Azerbaijan mud volcanoes detected through satellite radar interferometry (DInSAR). *Tectonophysics*, 637, pp.163-177.
- Askne, J.I., Fransson, J.E., Santoro, M., Soja, M.J. and Ulander, L.M., 2013. Model-based biomass estimation of a hemi-boreal forest from multitemporal TanDEM-X acquisitions. *Remote Sensing*, 5(11), pp.5574-5597.
- Bamler, Richard, and Philipp Hartl. "Synthetic aperture radar interferometry." *Inverse problems* 14, no. 4 (1998): R1.
- Berardino, P., Fornaro, G., Lanari, R. and Sansosti, E., 2002. A new algorithm for surface deformation monitoring based on small baseline differential SAR interferograms. *IEEE Transactions on Geoscience and Remote Sensing*, 40(11), pp.2375-2383.
- Bignami, C., 2012. Handbook for volcanic risk management: Prevention, crisis management and resilience. In *Handbook for volcanic risk management: Prevention, crisis management and resilience*. MiaVita. Bureau de Recherches Géologiques et Minières.
- Bonforte, Alessandro, et al. "Structural assessment of Mount Etna volcano from Permanent Scatterers analysis." *Geochemistry, Geophysics, Geosystems* 12.2 (2011).
- Briole, P., Massonnet, D. and Delacourt, C., 1997. Post-eruptive deformation associated with the 1986–87 and 1989 lava flows of Etna detected by radar interferometry. *Geophysical Research Letters*, 24(1), pp.37-40.
- Calais, E., Freed, A., Mattioli, G., Amelung, F., Jónsson, S., Jansma, P., Hong, S.H., Dixon, T., Prépetit, C. and Momplaisir, R., 2010. Transpressional rupture of an

- unmapped fault during the 2010 Haiti earthquake. *Nature Geoscience*, 3(11), pp.794-799.
- Costantini, M., 1998. A novel phase unwrapping method based on network programming. *IEEE Transactions on geoscience and remote sensing*, 36(3), pp.813-821.
- Crosetto, M., Crippa, B., Biescas, E., Monserrat, O. and Agudo, M., 2005, May. State of the art of land deformation monitoring using differential SAR interferometry. In ISPRS Hannover Workshop (pp. 17-20).
- Curlander, J.C. and McDonough, R.N., 1991. *Synthetic aperture radar* (p. 396). New York, NY, USA: John Wiley & Sons.
- Di Martire, D., Iglesias, R., Monells, D., Centolanza, G., Sica, S., Ramondini, M., Pagano, L., Mallorquí, J.J. and Calcaterra, D., 2014. Comparison between differential SAR interferometry and ground measurements data in the displacement monitoring of the earth-dam of Conza della Campania (Italy). *Remote sensing of environment*, 148, pp.58-69.
- Druitt, T.H., Edwards, L., Mellors, R.M., Pyle, D.M., Sparks, R.S.J., Lanphere, M., Davies, M. and Barreirio, B., 1999. Santorini volcano. *Geological Society Memoir*, 19.
- Ferretti, A., Monti-Guarnieri, A., Prati, C., Rocca, F. and Massonnet, D., 2007. InSAR principles-guidelines for SAR interferometry processing and interpretation (Vol. 19).
- Ferretti, A., Prati, C. and Rocca, F., 2000. Nonlinear subsidence rate estimation using permanent scatterers in differential SAR interferometry. *IEEE Transactions on Geoscience and Remote Sensing*, 38(5), pp.2202-2212.
- Foumelis, M., Trasatti, E., Papageorgiou, E., Stramondo, S. and Parcharidis, I., 2013. Monitoring Santorini volcano (Greece) breathing from space. *Geophysical Journal International*, p.ggs135.

- Fournier, T.J., Pritchard, M.E. and Riddick, S.N., 2010. Duration, magnitude, and frequency of subaerial volcano deformation events: New results from Latin America using InSAR and a global synthesis. *Geochemistry, Geophysics, Geosystems*, 11(1).
- Funning, G.J., Parsons, B., Wright, T.J., Jackson, J.A. and Fielding, E.J., 2005. Surface displacements and source parameters of the 2003 Bam (Iran) earthquake from Envisat advanced synthetic aperture radar imagery. *Journal of Geophysical Research: Solid Earth*, 110(B9).
- Ge, L., Chang, H.C. and Rizos, C., 2007. Mine subsidence monitoring using multi-source satellite SAR images. *Photogrammetric Engineering & Remote Sensing*, 73(3), pp.259-266.
- Georgalas, G.C., 1962. *Catalogue of the Active Volcanoes of the World Including Solfatara Fields: Greece*. International Association of Volcanology.
- Goel, K., Adam, N. and Minet, C., 2011, September. Long term analysis of strong non-linear deformations induced by coal mining using the SBAS technique. In *ESA Fringe Symp* (pp. 19-23).
- Goldstein, R.M. and Werner, C.L., 1998. Radar interferogram filtering for geophysical applications. *Geophysical Research Letters*, 25(21), pp.4035-4038.
- Hanssen, R.F., 2001. Radar interferometry: data interpretation and error analysis (Vol. 2). Springer Science & Business Media.
- Hanssen, R.F., 2005. Satellite radar interferometry for deformation monitoring: a priori assessment of feasibility and accuracy. *International journal of applied earth observation and geoinformation*, 6(3), pp.253-260.
- Hooper, A., Prata, F. and Sigmundsson, F., 2012. Remote sensing of volcanic hazards and their precursors. *Proceedings of the IEEE*, 100(10), pp.2908-2930.
- Hooper, A., Segall, P. and Zebker, H., 2007. Persistent scatterer interferometric synthetic aperture radar for crustal deformation analysis, with application to

Volcán Alcedo, Galápagos. *Journal of Geophysical Research: Solid Earth*, 112(B7).

Huijsmans, J.P.P., 1985. Calc-alkaline lavas from the volcanic complex of Santorini, Aegean Sea, Greece: a petrological, geochemical and stratigraphic study. *Geologica Ultraiectina*, 41, pp.1-316.

Lagios, E., Sakkas, V., Novali, F., Bellotti, F., Ferretti, A., Vlachou, K. and Dietrich, V., 2013. SqueeSAR™ and GPS ground deformation monitoring of Santorini Volcano (1992–2012): tectonic implications. *Tectonophysics*, 594, pp.38-59.

Lanari, R., Lundgren, P. and Sansosti, E., 1998. Dynamic deformation of Etna volcano observed by satellite radar interferometry. *Geophysical Research Letters*, 25(10), pp.1541-1544.

Liu, P., Li, Z., Hoey, T., Kincal, C., Zhang, J., Zeng, Q. and Muller, J.P., 2013. Using advanced InSAR time series techniques to monitor landslide movements in Badong of the Three Gorges region, China. *International Journal of Applied Earth Observation and Geoinformation*, 21, pp.253-264.

Manning, S.W., Ramsey, C.B., Kutschera, W., Higham, T., Kromer, B., Steier, P. and Wild, E.M., 2006. Chronology for the Aegean Late Bronze Age 1700-1400 BC. *Science*, 312(5773), pp.565-569.

Massonnet, D. and Feigl, K.L., 1998. Radar interferometry and its application to changes in the Earth's surface. *Reviews of geophysics*, 36(4), pp.441-500

Massonnet, D., Briole, P. and Arnaud, A., 1995. Deflation of Mount Etna monitored by spaceborne radar interferometry. *Nature*, 375(6532), pp.567-570.

McCoy, F.W. and Heiken, G., 2000. Tsunami generated by the Late Bronze age eruption of Thera (Santorini), Greece. *Pure and Applied Geophysics*, 157(6-8), pp.1227-1256.

Moreira, A., 2014, June. A golden age for spaceborne SAR systems. In *Microwaves, Radar, and Wireless Communication (MIKON), 2014 20th International Conference on* (pp. 1-4). IEEE.

- Newman, A.V., Stiros, S., Feng, L., Psimoulis, P., Moschas, F., Saltogianni, V., Jiang, Y., Papazachos, C., Panagiotopoulos, D., Karagianni, E. and Vamvakaris, D., 2012. Recent geodetic unrest at Santorini caldera, Greece. *Geophysical Research Letters*, 39(6).
- Nomikou, P., Parks, M.M., Papanikolaou, D., Pyle, D.M., Mather, T.A., Carey, S., Watts, A.B., Paulatto, M., Kalnins, M.L., Livanos, I. and Bejelou, K., 2014. The emergence and growth of a submarine volcano: The Kameni islands, Santorini (Greece). *GeoResJ*, 1, pp.8-18.
- Papoutsis, I., Papanikolaou, X., Floyd, M., Ji, K.H., Kontoes, C., Paradissis, D. and Zacharis, V., 2013. Mapping inflation at Santorini volcano, Greece, using GPS and InSAR. *Geophysical Research Letters*, 40(2), pp.267-272.
- Paradella, Waldir R., et al. "Mapping surface deformation in open pit iron mines of Carajás Province (Amazon Region) using an integrated SAR analysis." *Engineering Geology* 193 (2015): 61-78.
- Parcharidis, I., Fomelis, M., Benekos, G., Kourkouli, P., Stamatopoulos, C. and Stramondo, S., 2015. Time series synthetic aperture radar interferometry over the multispan cable-stayed Rio-Antirio Bridge (central Greece): achievements and constraints. *Journal of Applied Remote Sensing*, 9(1), pp.096082-096082.
- Parcharidis, I., Lagios, E., Sakkas, V., Raucoules, D., Feurer, D., Le Mouélic, S., King, C., Carnec, C., Novali, F., Ferretti, A. and Capes, R., 2006. Subsidence monitoring within the Athens basin (Greece) using space radar interferometric techniques. *Earth, planets and space*, 58(5), pp.505-513.
- Parks, M.M., Biggs, J., England, P., Mather, T.A., Nomikou, P., Palamartchouk, K., Papanikolaou, X., Paradissis, D., Parsons, B., Pyle, D.M. and Raptakis, C., 2012. Evolution of Santorini Volcano dominated by episodic and rapid fluxes of melt from depth. *Nature Geoscience*, 5(10), pp.749-754.
- Parks, M.M., Moore, J.D., Papanikolaou, X., Biggs, J., Mather, T.A., Pyle, D.M., Raptakis, C., Paradissis, D., Hooper, A., Parsons, B. and Nomikou, P., 2015. From quiescence to unrest: 20 years of satellite geodetic measurements at Santorini

volcano, Greece. *Journal of Geophysical Research: Solid Earth*, 120(2), pp.1309-1328.

Prats-Iraola, P., Nannini, M., Scheiber, R., De Zan, F., Wollstadt, S., Minati, F., Vecchioli, F., Costantini, M., Borgstrom, S., De Martino, P. and Siniscalchi, V., 2015, July. Sentinel-1 assessment of the interferometric wide-swath mode. In *2015 IEEE International Geoscience and Remote Sensing Symposium (IGARSS)* (pp. 5247-5251). IEEE.

Pyle, D.M. and Elliott, J.R., 2006. Quantitative morphology, recent evolution, and future activity of the Kameni Islands volcano, Santorini, Greece. *Geosphere*, 2(5), pp.253-268.

Quincey, D.J., Luckman, A. and Benn, D., 2009. Quantification of Everest region glacier velocities between 1992 and 2002, using satellite radar interferometry and feature tracking. *Journal of Glaciology*, 55(192), pp.596-606.

Raucoules, D., Le Mouélic, S., Carnec, C., Maisons, C. and King, C., 2003. Urban subsidence in the city of Prato (Italy) monitored by satellite radar interferometry. *International journal of remote sensing*, 24(4), pp.891-897.

Raucoules, D., Parcharidis, I., Feurer, D., Novalli, F., Ferretti, N., Carnec, C., Lagios, E., Sakkas, V., Le Mouélic, S., Cooksley, G. and Hosford, S., 2008. Ground deformation detection of the greater area of Thessaloniki (Northern Greece) using radar interferometry techniques. *Natural Hazards and Earth System Sciences*, 8(4), pp.779-788.

Rosen, P.A., Hensley, S., Joughin, I.R., Li, F.K., Madsen, S.N., Rodriguez, E. and Goldstein, R.M., 2000. Synthetic aperture radar interferometry. *Proceedings of the IEEE*, 88(3), pp.333-382.

Sigurdsson, H. and Carey, S., 1989. Plinian and co-ignimbrite tephra fall from the 1815 eruption of Tambora volcano. *Bulletin of Volcanology*, 51(4), pp.243-270.

Sigurdsson, H., Carey, S., Alexandri, M., Vougioukalakis, G., Croff, K., Roman, C., Sakellariou, D., Anagnostou, C., Rousakis, G., Ioakim, C. and Goguo, A., 2006.

- Marine investigations of Greece's Santorini volcanic field. *EOS, Transactions American Geophysical Union*, 87(34), pp.337-342
- Solaro, G., Acocella, V., Pepe, S., Ruch, J., Neri, M. and Sansosti, E., 2010. Anatomy of an unstable volcano from InSAR: Multiple processes affecting flank instability at Mt. Etna, 1994–2008. *Journal of Geophysical Research: Solid Earth*, 115(B10).
- Strozzi, T., Kouraev, A., Wiesmann, A., Wegmüller, U., Sharov, A. and Werner, C., 2008. Estimation of Arctic glacier motion with satellite L-band SAR data. *Remote Sensing of Environment*, 112(3), pp.636-645.
- Strozzi, T., Tazlo, et al. "Land subsidence monitoring with differential SAR interferometry." *Photogrammetric engineering and remote sensing* 67.11 (2001): 1261-1270.
- Wegmüller, U., Santoro, M., Werner, C. and Cartus, O., 2015a. On the Estimation and Interpretation of Sentinel-1 TOPS InSAR Coherence. *Proc. of FRINGE, ESA SP-731 (CD-ROM), ESA Publications Division, European Space Agency, Noordwijk, The Netherlands*.
- Wegmüller, U., Werner, C., Strozzi, T., Wiesmann, A., Frey, O. and Santoro, M., 2015b, March. Sentinel-1 support in the gamma software. In *Proceedings of the Fringe 2015 Conference, ESA ESRIN, Frascati, Italy* (pp. 23-27).
- Werner, C., Wegmüller, U., Strozzi, T. and Wiesmann, A., 2002, June. Processing strategies for phase unwrapping for INSAR applications. In *Proceedings of the European Conference on Synthetic Aperture Radar EUSAR*.
- Yagüe-Martínez, N., Prats-Iraola, P., Gonzalez, F.R., Brcic, R., Shau, R., Geudtner, D., Eineder, M. and Bamler, R., 2016. Interferometric Processing of Sentinel-1 TOPS Data. *IEEE Transactions on Geoscience and Remote Sensing*, 54(4), pp.2220-2234.
- Zebker, H.A., Rosen, P.A. and Hensley, S., 1997. Atmospheric effects in interferometric synthetic aperture radar surface deformation and topographic maps. *Journal of Geophysical Research: Solid Earth*, 102(B4), pp.7547-7563.

Zhou, X., Chang, N.B. and Li, S., 2009. Applications of SAR interferometry in earth and environmental science research. *Sensors*, 9(3), pp.1876-1912.

Publication List

Institutionen för naturgeografi och ekosystemvetenskap, Lunds Universitet.

Student examensarbete (Seminarieuppsatser). Uppsatserna finns tillgängliga på institutionens geobibliotek, Sölvegatan 12, 223 62 LUND. Serien startade 1985. Hela listan och själva uppsatserna är även tillgängliga på LUP student papers (<https://lup.lub.lu.se/student-papers/search/>) och via Geobiblioteket (www.geobib.lu.se)

The student thesis reports are available at the Geo-Library, Department of Physical Geography and Ecosystem Science, University of Lund, Sölvegatan 12, S-223 62 Lund, Sweden. Report series started 1985. The complete list and electronic versions are also electronic available at the LUP student papers (<https://lup.lub.lu.se/student-papers/search/>) and through the Geo-library (www.geobib.lu.se)

- 350 Mihaela – Mariana Tudoran (2015) Occurrences of insect outbreaks in Sweden in relation to climatic parameters since 1850
- 351 Maria Gatzouras (2015) Assessment of trampling impact in Icelandic natural areas in experimental plots with focus on image analysis of digital photographs
- 352 Gustav Wallner (2015) Estimating and evaluating GPP in the Sahel using MSG/SEVIRI and MODIS satellite data
- 353 Luisa Teixeira (2015) Exploring the relationships between biodiversity and benthic habitat in the Primeiras and Segundas Protected Area, Mozambique
- 354 Iris Behrens & Linn Gardell (2015) Water quality in Apac-, Mbale- & Lira district, Uganda - A field study evaluating problems and suitable solutions
- 355 Viktoria Björklund (2015) Water quality in rivers affected by urbanization: A Case Study in Minas Gerais, Brazil

- 356 Tara Mellquist (2015) Hållbar dagvattenhantering i Stockholms stad - En riskhanteringsanalys med avseende på långsiktig hållbarhet av Stockholms stads dagvattenhantering i urban miljö
- 357 Jenny Hansson (2015) Trafikrelaterade luftföroreningar vid förskolor – En studie om kvävedioxidhalter vid förskolor i Malmö
- 358 Laura Reinelt (2015) Modelling vegetation dynamics and carbon fluxes in a high Arctic mire
- 359 Emelie Linnéa Graham (2015) Atmospheric reactivity of cyclic ethers of relevance to biofuel combustion
- 360 Filippo Gualla (2015) Sun position and PV panels: a model to determine the best orientation
- 361 Joakim Lindberg (2015) Locating potential flood areas in an urban environment using remote sensing and GIS, case study Lund, Sweden
- 362 Georgios-Konstantinos Lagkas (2015) Analysis of NDVI variation and snowmelt around Zackenberg station, Greenland with comparison of ground data and remote sensing.
- 363 Carlos Arellano (2015) Production and Biodegradability of Dissolved Organic Carbon from Different Litter Sources
- 364 Sofia Valentin (2015) Do-It-Yourself Helium Balloon Aerial Photography - Developing a method in an agroforestry plantation, Lao PDR
- 365 Shirin Danehpash (2015) Evaluation of Standards and Techniques for Retrieval of Geospatial Raster Data - A study for the ICOS Carbon Portal
- 366 Linnea Jonsson (2015) Evaluation of pixel based and object based classification methods for land cover mapping with high spatial resolution satellite imagery, in the Amazonas, Brazil.
- 367 Johan Westin (2015) Quantification of a continuous-cover forest in Sweden using remote sensing techniques

- 368 Dahlia Mudzaffar Ali (2015) Quantifying Terrain Factor Using GIS Applications for Real Estate Property Valuation
- 369 Ulrika Belsing (2015) The survival of moth larvae feeding on different plant species in northern Fennoscandia
- 370 Isabella Grönfeldt (2015) Snow and sea ice temperature profiles from satellite data and ice mass balance buoys
- 371 Karolina D. Pantazatou (2015) Issues of Geographic Context Variable Calculation Methods applied at different Geographic Levels in Spatial Historical Demographic Research -A case study over four parishes in Southern Sweden
- 372 Andreas Dahlbom (2016) The impact of permafrost degradation on methane fluxes - a field study in Abisko
- 373 Hanna Modin (2016) Higher temperatures increase nutrient availability in the High Arctic, causing elevated competitive pressure and a decline in *Papaver radicum*
- 374 Elsa Lindevall (2016) Assessment of the relationship between the Photochemical Reflectance Index and Light Use Efficiency: A study of its seasonal and diurnal variation in a sub-arctic birch forest, Abisko, Sweden
- 375 Henrik Hagelin and Matthieu Cluzel (2016) Applying FARSITE and Prometheus on the Västmanland Fire, Sweden (2014): Fire Growth Simulation as a Measure Against Forest Fire Spread – A Model Suitability Study –
- 376 Pontus Cederholm (2016) Californian Drought: The Processes and Factors Controlling the 2011-2016 Drought and Winter Precipitation in California
- 377 Johannes Loer (2016) Modelling nitrogen balance in two Southern Swedish spruce plantations
- 378 Hanna Angel (2016) Water and carbon footprints of mining and producing Cu, Mg and Zn: A comparative study of primary and secondary sources

- 379 Gusten Brodin (2016) Organic farming's role in adaptation to and mitigation of climate change - an overview of ecological resilience and a model case study
- 380 Verånika Trollblad (2016) Odling av Cucumis Sativus L. med aska från träd som näringstillägg i ett urinbaserat hydroponiskt system
- 381 Susanne De Bourg (2016) Tillväxteffekter för andra generationens granskog efter tidigare genomförd kalkning
- 382 Katarina Crafoord (2016) Placering av energiskog i Sverige - en GIS analys
- 383 Simon Nåfält (2016) Assessing avalanche risk by terrain analysis An experimental GIS-approach to The Avalanche Terrain Exposure Scale (ATES)
- 384 Vide Hellgren (2016) Asteroid Mining - A Review of Methods and Aspects
- 385 Tina Truedsson (2016) Hur påverkar snömängd och vindförhållande vattentrycksmätningar vintertid i en sjö på västra Grönland?
- 386 Chloe Näslund (2016) Prompt Pediatric Care Pediatric patients' estimated travel times to surgically-equipped hospitals in Sweden's Scania County
- 387 Yufei Wei (2016) Developing a web-based system to visualize vegetation trends by a nonlinear regression algorithm
- 388 Greta Wistrand (2016) Investigating the potential of object-based image analysis to identify tree avenues in high resolution aerial imagery and lidar data
- 389 Jessica Ahlgren (2016) Development of a Web Mapping Application for grazing resource information in Kordofan, Sudan, by downloading MODIS data automatically via Python
- 390 Hanna Axén (2016) Methane flux measurements with low-cost solid state sensors in Kobbefjord, West Greenland
- 391 Ludvig Forslund (2016) Development of methods for flood analysis and response in a Web-GIS for disaster management

- 392 Shuzhi Dong (2016) Comparisons between different multi-criteria decision analysis techniques for disease susceptibility mapping
- 393 Thirze Hermans (2016) Modelling grain surplus/deficit in Cameroon for 2030
- 394 Stefanos Georganos (2016) Exploring the spatial relationship between NDVI and rainfall in the semi-arid Sahel using geographically weighted regression
- 395 Julia Kelly (2016) Physiological responses to drought in healthy and stressed trees: a comparison of four species in Oregon, USA
- 396 Antonín Kusbach (2016) Analysis of Arctic peak-season carbon flux estimations based on four MODIS vegetation products
- 397 Luana Andreea Simion (2016) Conservation assessments of Văcărești urban wetland in Bucharest (Romania): Land cover and climate changes from 2000 to 2015
- 398 Elsa Nordén (2016) Comparison between three landscape analysis tools to aid conservation efforts
- 399 Tudor Buhalău (2016) Detecting clear-cut deforestation using Landsat data: A time series analysis of remote sensing data in Covasna County, Romania between 2005 and 2015
- 400 Sofia Sjögren (2016) Effective methods for prediction and visualization of contaminated soil volumes in 3D with GIS
- 401 Jayan Wijesingha (2016) Geometric quality assessment of multi-rotor unmanned aerial vehicle-borne remote sensing products for precision agriculture
- 402 Jenny Ahlstrand (2016) Effects of altered precipitation regimes on bryophyte carbon dynamics in a Peruvian tropical montane cloud forest
- 403 Peter Markus (2016) Design and development of a prototype mobile geographical information system for real-time collection and storage of traffic accident data

404 Christos Bountzouklis (2016) Monitoring of Santorini (Greece) volcano during post-unrest period (2014-2016) with Interferometric Time series of Sentinel-1A